

**PROBING WATER DYNAMICS IN CELLULOSE STRUCTURES USING
TERAHERTZ SPECTROSCOPY**

by

Lovepreet Kaur

B.Sc., Physics (Hons.), Khalsa College Amritsar, 2019

THESIS SUBMITTED IN PARTIAL FULFILLMENT OF
THE REQUIREMENTS FOR THE DEGREE OF
MASTER OF SCIENCE
IN
PHYSICS

UNIVERSITY OF NORTHERN BRITISH COLUMBIA

March 2024

© Lovepreet Kaur, 2024

UNIVERSITY OF NORTHERN BRITISH COLUMBIA PARTIAL COPYRIGHT LICENCE

I hereby grant the University of Northern British Columbia the right to lend my project/thesis/dissertation to users of the library or to other libraries. Furthermore, I grant the University of Northern British Columbia library the right to make single copies only of my project/thesis/dissertation for users of the library or in response to a request from other libraries, on their behalf or one of their users. Permission for extensive copying of this project/thesis/dissertation for scholarly purposes may be granted by me or by a member of the university designated by me. It is understood that copying or publication of this thesis/dissertation for financial gain shall not be allowed without my written permission.

Title of Project/Thesis/Dissertation:

Probing water dynamics in Cellulose structures using Terahertz Spectroscopy

Author: Lovepreet Kaur

Signature: _____

Date: March 2024

Abstract

Terahertz time-domain spectroscopy was used to probe water dynamics in microcrystalline cellulose. In this study, the variation of the dielectric constant of water in microcrystalline cellulose samples with moisture contents between 2.65% and 16.73% was studied. It was found that the dielectric function of water does change with a change in moisture content in microcrystalline cellulose. The dielectric function of water appears to change from what might be expected for bound water towards values that are more consistent with bulk water at higher moisture content. This study is a step forward in the direction of understanding if the dielectric function of water goes from bound to free with a change in moisture content in microcrystalline cellulose. Future work to understand the detailed behavior of this transition is important for wood science and THz application to wood science.

LIST OF CONTRIBUTIONS

Journal Articles

- [A1] M. Reid, M. Gehloff, I. D. Hartley, L. Mucchi, and L. Kaur, "100 GHz phase contrast scanner for measuring density and thickness," to be published.

Conference Presentations

- [C1] L. Kaur, M. Gehloff, I. D. Hartley, and M. Reid, "Terahertz non-destructive testing for industrial manufacturing", Women in Physics Canada conference, 2023, Manitoba, Canada.

TABLE OF CONTENTS

Abstract	iii
List of Contributions	iv
Table of Contents	v
List of Tables	vi
List of Figures	vii
List of Abbreviations	xi
Acknowledgements	xii
Dedication	xiii
1 Introduction	1
1.1 Overview and Motivation	3
1.1.1 Motivation	3
1.1.2 Overview of thesis and upcoming chapters	4
2 Terahertz Time Domain Spectroscopy (THz-TDS); Background	6
2.1 Terahertz Time Domain Spectroscopy (THz-TDS)	7
2.2 THz radiation emission	9
2.2.1 Generation of THz using photoconductive antennas	10
2.3 Detection of THz using photoconductive sampling	11
2.4 Using THz radiation to probe samples	12
2.5 Analysis of the data	12
2.5.1 Duvillaret's Method	13
2.5.2 The Numerical Method	18
3 Microcrystalline Cellulose: Structure and Interaction with Water	25
3.1 Abstract	25
3.2 Introduction	25
3.3 Materials and methods	33

3.3.1	Sorption isotherm	33
3.3.2	Nitrogen sorption	34
3.3.3	Thermogravimetric Analysis (TGA)	35
3.4	Results and discussion	35
3.5	Summary	39
4	Probing Water Dynamics in MCC using THz-TDS	41
4.1	Abstract	41
4.2	Introduction	42
4.2.1	Effective Medium Theory	43
4.2.1.1	Maxwell-Garnet Effective Medium Theory	44
4.2.1.2	Bruggman model	45
4.2.1.3	Parallel model: simple effective medium theory	46
4.3	Materials and Methods	50
4.3.1	Sample preparation	51
4.3.2	THz spectral measurements	52
4.4	Results and Discussion	54
4.4.0.1	Prediction of the dielectric function of bound water from THz measurements	61
4.5	Summary	69
5	Conclusion and Future Directions	70
	Bibliography	73

LIST OF TABLES

3.1	Saturated salt solutions and their corresponding RH% used to study moisture sorption by the MCC samples.	34
4.1	Saturated salt solutions and their corresponding RH% used for conditioning the MCC samples.	51
4.2	The four ranges of MC and the associated type of moisture with them. As adapted from Torgovnikov G.I. 1993	57

LIST OF FIGURES

1.1	The Electromagnetic spectrum.	2
2.1	THz time-domain signals with and without using a 4.4 mm thick oven-dried microcrystalline powder in a petri dish. This Figure clearly indicates the change in amplitude (lower amplitude for sample waveform as compared to reference due to radiation absorption by cellulose powder) and a phase shift (waveform comes later in time (a time delay) due to the slower propagation speed of radiation in the cellulose powder as compared to air).	8
2.2	The experimental setup of THz-TDS. The femtosecond (fs) laser beam output is divided into two parts with the help of a beam splitter. One part of the beam is used to generate the THz radiation, and the other half is passed through the delay line and used to detect the THz beam. The probe beam gates the photoconductive detector, which overlaps the created THz pulse. The field is mapped out in time by varying the optical delay between the gating optical pulse and the THz pulse being detected.	9
2.3	The configuration for transmission spectroscopy: T_x represents a transmitter and R_x represents a receiver.	13
2.4	Variation of the amplitude of the THz beam in the presence and absence of sample with respect to time for paper. Red line: reference THz beam, and blue line: beam in the presence of the sample. . . .	16
2.5	Variation of Index of refraction with respect to frequency by calculating the mean (red) and standard deviation (black) for five runs for 20 sheets of paper as a sample.	17
2.6	Variation of absorption coefficient with change in frequency by calculation mean and standard deviation for five runs for 20 sheets of paper as a sample.	18
2.7	The representation of Fabry-Perot reflections from the incident electric field $E(\text{init})$ transmitting through the sample with a different refractive index that is surrounded by air. T_x represents a transmitter and R_x represents a receiver.	20
2.8	Index of refraction for 20 sheets of paper as a sample using Koch's method.	23

2.9	Absorption coefficient for 20 sheets of paper as a sample using Koch's method.	24
3.1	Flowchart of the chemical composition of wood.	26
3.2	The chemical constitution of cellulose. (a) Molecule of β -glucose (b) representation of part of the cellulose molecule, a 1-4 polymer of β -glucose.	28
3.3	The manufacturing process of MCC from the cellulose sources. As adapted from: Trache et al. 2016	30
3.4	Variation of MC (oven-dry basis) in MCC as a function of RH.	36
3.5	Fit of BET equation to water vapor sorption data for MCC. The value of $n = 1$ represents the monomolecular layer. It is also been plotted for the $n= 10$ number of layers.	37
3.6	TGA analysis of MCC sample. Run (a) TGA performed at rate of 1° C Run (b) TGA performed at rate of 10° C.	38
4.1	Pictorial representation of a three-phase striped composite medium, where red arrow indicates the direction of the electric field.	47
4.2	Flowchart showing the step-wise process of sample preparation to THz spectral measurements.	53
4.3	The representation of basic setup used to make THz spectral measurements of MCC samples.	54
4.4	The flowchart shows the measurement process of obtaining the dielectric constant of water using the THz spectral measurements.	55
4.5	Variation of THz field amplitude in time for variable MC in MCC samples. As the MC gets higher in MCC samples, the THz field amplitude decreases, and the THz pulse comes later in time (phase shift or time delay).	56
4.6	Variation of the real part of the dielectric function of MCC with respect to frequency obtained using THz transmission spectroscopy. This figure shows the real part of the dielectric function of MCC increases with an increase in MC.	58
4.7	Variation of the imaginary part of the dielectric function of MCC with respect to frequency obtained using THz transmission spectroscopy. This figure shows the imaginary part of the dielectric function of MCC increasing with increasing MC.	59
4.8	Variation of the real part of the dielectric function of MCC with respect to MC(%) obtained using THz transmission spectroscopy at a frequency of 0.2 THz.	60
4.9	Variation of the imaginary part of the dielectric function of MCC with respect to MC(%) obtained using THz transmission spectroscopy at a frequency of 0.2 THz.	61
4.10	Variation of the real part of the dielectric function of water with respect to frequency obtained using THz transmission spectroscopy.	63

4.11	Variation of the imaginary part of the dielectric function of water with respect to frequency obtained using THz transmission spectroscopy.	64
4.12	Variation of the real part of the dielectric function of water with respect to MC obtained using THz transmission spectroscopy at 0.2 THz.	67
4.13	Variation of the imaginary part of the dielectric function of water with respect to MC obtained using THz transmission spectroscopy at 0.2 THz.	68

LIST OF ABBREVIATIONS

THz	Terahertz
RH	Relative Humidity
THz-TDS	Terahertz Time Domain Spectroscopy
MCC	Microcrystalline Cellulose
MC	Moisture Content
EMC	Equilibrium Moisture Content
TGA	Thermogravimetric Analysis
J	Photocurrent
E	Electric field amplitude
ν	Frequency
L	Thickness of the sample
\hat{t}_{ij}	Fresnel Transmission Coefficients
\hat{n}_b	Complex index of refraction of material b
n	Index of refraction
α	Absorption coefficient
m	Wet mass of sample
m_{od}	Oven-dried mass of sample
M_m	Moisture adsorbed by monolayer
c	Speed of light
ρ	Density
f_i	Volume fraction of component i
ϵ	Permittivity

Acknowledgements

"O Nanak, don't be anxious; the Lord will take care of you."

I would like to express my deep gratitude to my supervisor, Dr. Matthew Reid, for giving me an opportunity to do research under his supervision and providing me with invaluable guidance throughout this journey. I consider myself lucky to be a part of his team and work alongside him.

I would also like to acknowledge significant support from my co-supervisor, Dr. Ian Hartley. This work would not have been possible without the expertise provided by Dr. Hartley. I am grateful for the financial support and research opportunities provided to me by both of my supervisors.

I would also like to thank my supervisory committee member, Dr. Kerry Reimer, for his feedback throughout my thesis project. I would like to thank Dr. Erik Jensen and the entire Physics Department for supporting me in attending my first-ever conference in Canada. I would also like to thank and appreciate Dr. Maik Gehloff and the researchers at the Wood Innovation Research Lab (WIRL), UNBC, for their constant help and support during the conduct of my thesis experiments. I would also like to thank my friends at school, especially Abid Afzal, for his help along the way.

Finally, my heartfelt appreciation goes to my parents, S. Ajit Singh and Mrs. Parmjit Kaur, for their unconditional love and support. I would like to thank my sister, Navjot Kaur, and brother, Dr. Ranjodh Singh, and my wonderful in-laws, Mrs. Daljit Kaur, and S. Sulakhan Singh, for their unconditional support along the way. Finally, I would like to thank my wonderful husband, S. Jaskaran Singh, for being on my side throughout this period of my life.

Dedication

To my parents,
S. Ajit Singh
and
Mrs. Parmjit Kaur,
who are always there when I need them.

Chapter 1

Introduction

Terahertz (THz) radiation occupies the far-infrared portion of the electromagnetic spectrum, lying between the microwave and infrared regions [1] [2], as represented in Figure 1.1. Its wavelengths fall within the sub-mm range, enabling high-resolution imaging. Spectroscopic information, unattainable at lower frequencies like microwaves, becomes accessible in the THz region, and the shorter wavelength facilitates sub-mm imaging of materials.

THz radiation is non-ionizing, presenting minimal health concerns and making it safe for use on organic tissues [3] [4]. This property has led to its widespread application in non-destructive material evaluation. In comparison to X-rays, which also offer good spatial resolution, THz radiation's non-invasive and non-ionizing nature enhances safety [5].

This radiation is extensively utilized in pharmaceuticals and medical imaging [6] [7], such as the detection and imaging of breast cancer [4] and the determination of spectroscopic features of blood cells. Its ability to pass through fabrics and plastics makes it valuable in explosives and weapons surveillance [8] [9], especially in security-critical locations like airports. Despite its limited penetration into the human body, THz radiation remains safe for use on human subjects [10].

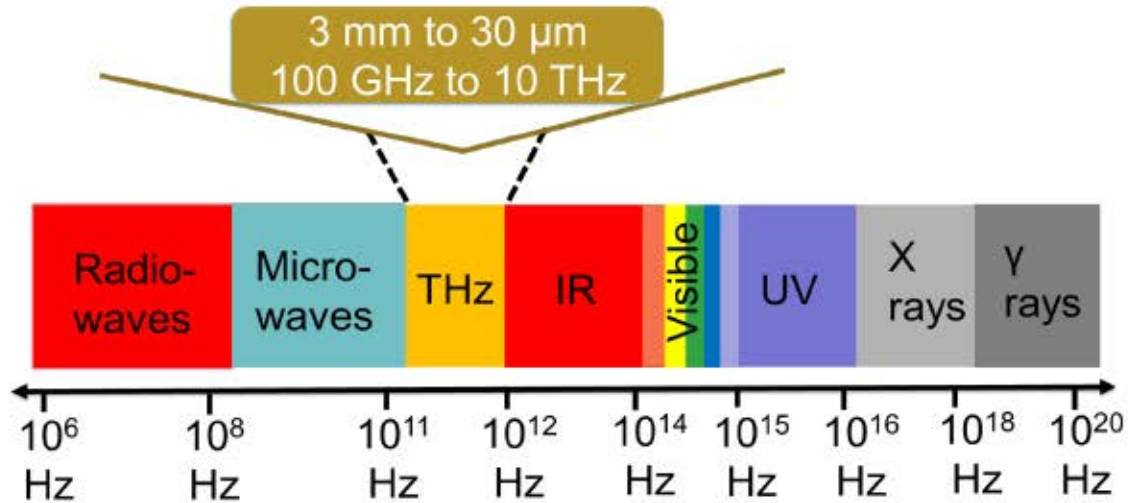


Figure 1.1: The Electromagnetic spectrum.

The THz frequency range spans from 0.1 to 10 THz, characterized by sub-millimeter wavelengths that provide superior spatial resolution compared to microwaves. Its non-ionizing nature and transparency in dry materials make it valuable for transmission imaging. However, THz radiation has limitations, including interactions with polar molecules and absorption by water.

In the field of wood science, the THz region, specifically below 1 THz, is crucial [11] [12]. THz radiation is sensitive to the internal fiber structure of wood and wood products, offering new applications in the wood industry [13]. Materials like wood composites, papers [14], and ceramic knives are transparent in this region, facilitating the identification and imaging of various materials.

Wood is a hygroscopic material, and chemically, it is mainly composed of cellulose, hemicelluloses, and lignin [15]. Out of these three components, cellulose ($C_6H_{10}O_5$)_n is the main component with 65-70% polysaccharide substance and is composed of a linear chain of glucose monomers. Wood is opaque in the ultraviolet, visible, and infrared, and its imaging is limited to reflection geometries in these regions of the electromagnetic spectrum [16]. On the other hand, wood is transparent at X-ray and microwave frequencies, and measurements can be ob-

tained in transmission [17] [18]. Sub-annual ring resolution cannot be achieved with GHz-frequency microwaves (\sim cm wavelengths), and safety regulations need to be in place using X-rays because X-rays are hazardous to health. Therefore, it is helpful to introduce new imaging techniques with good spatial resolution that are non-destructive and safe to work with [19].

In wood science [20] [21], research often employs techniques like THz Time-Domain Spectroscopy (THz-TDS) to understand water-wood interactions. This study focuses on microcrystalline cellulose (MCC) as a model material, simplifying investigations into water-cellulose interactions due to its well-defined crystalline structure. Therefore, in this thesis, THz time-domain spectroscopy (THz-TDS) (details in Chapter 2) was performed on MCC in a transmission geometry. THz-TDS has already been used for cellulose research to quantify the degree of crystallinity of MCC [22] [23] [24] [25]. Moreover, the analysis and interpretation of the spectroscopic characterization of paper properties, such as paper type [14], moisture content (MC), and orientation, based on the Lorentz-Lorenz and Clausius-Mosotti relations, have been made using THz-TDS [26] [27]. Thus, understanding water interactions with cellulose/MCC has implications for fundamental wood science and industrial applications. This knowledge contributes to the optimization of wood processing and product quality. The study of moisture interaction in wood and cellulose-based materials enhances our understanding of their behavior, leading to advancements in materials science and environmental engineering.

1.1 Overview and Motivation

1.1.1 Motivation

Cellulose is a polysaccharide substance $(C_6H_{10}O_5)_n$ composed of a linear chain of glucose monomers. As an organic substance making up most of a plant's cell

walls, it is one of Earth's most abundant natural and renewable biopolymers [28] [29]. The structure of cellulose chains consists of two intramolecular hydrogen bonds, OH-3...O5 and OH-2...O6, that can bind neighboring glucose units and thus provide high stiffness of natural cellulose chains [23] [30]. Wherever it is used, it is in contact with water vapor at different relative humidities (RHs) [31]. There have been a vast number of publications on cellulose-water interactions [30] [28], but the exact mechanisms of those interactions are not fully understood yet. One of the main reasons given for that is the wide variety of cellulose materials and sources [30], e.g., wood cellulose, bacterial cellulose, MCC, etc. Therefore, it is interesting to see the interactions of water vapors with cellulose at different levels of RH and how the dielectric function of water varies with the change in hydration level: this problem is the subject of this thesis.

1.1.2 Overview of thesis and upcoming chapters

In this thesis, THz spectroscopy was used to perform transmission measurements in the far-infrared range of the electromagnetic spectrum. THz radiation strongly gets absorbed by water; therefore, THz radiation offers the possibility to probe MC. Thus, in this thesis, THz-TDS is used to probe water dynamics in MCC and see the effect of MC on the dielectric function of water in cellulose networks.

To achieve the goal of this thesis, some systematic studies and steps were performed. The details of the system and technology used in this thesis are discussed in Chapter 2. It also introduces the working principles and applications of the THz-TDS. Moreover, this chapter discusses the methods of analysis, namely Duvillaret's and Koch's, that can be used to analyze the MCC samples used in this thesis and get important parameters like the index of refraction and absorption coefficient of MCC. The preliminary data analyzed is discussed and compared for the paper as a sample by using these two different analysis methods, which will then be used

to study the dielectric function of water in MCC.

Chapter 3 provides detailed insights into the structure of MCC and its generation from wood. As moisture in industrial wood is a very important factor, some details about the structure of wood and its components are also discussed. To thoroughly understand the interaction of water molecules with cellulose networks, the BET sorption theory is used. The understanding of the results was obtained using BET theory and then compared with the THz-TDS of MCC.

In Chapter 4, the dielectric function of water in MCC using THz-TDS is studied. Also, this chapter provides an answer to one of the very important questions in this thesis: How does the dielectric function of water vary by changing MC? The obtained dielectric function of water was compared with the dielectric function of free water and ice to understand the nature of the water molecules associated with the cell wall.

Chapter 5 concludes this thesis and also gives some future recommendations to improve the quality of work in this field of study.

Chapter 2

Terahertz Time Domain Spectroscopy (THz-TDS); Background

THz radiation is strongly absorbed by water [20] and is sensitive to the internal fibre structure of wood and its components [32]. The useful frequency range for wood science falls below 1 THz [21]. Therefore, it can be used to determine the MC of wood and its components, for example, cellulose, hemicellulose, and lignin. In this thesis, THz-TDS was performed to exploit THz technology for the determination of MCC in MCC, the most purified form of cellulose. To study moisture sorption in MCC, the index of refraction and absorption coefficient of MCC samples at various MCs is required. The index of refraction and absorption coefficient can then be used to get the complex index of refraction of water present in MCC. In the following sections of this chapter, the working principle and applications of THz-TDS are discussed. This chapter also discusses the method of analysis that we can use to get the index of refraction and absorption coefficient of MCC.

2.1 Terahertz Time Domain Spectroscopy (THz-TDS)

We can conduct THz transmission spectroscopy in the time and frequency domains, with the latter achieved through the Fourier transformation of the data measured in the time domain. THz-TDS is the method used in this thesis. THz systems generally employ coherent detection, often using photoconductive antennas. All measurements made in this thesis are conducted by measuring the electric field as a function of time, and the measurements are made directly in the time domain. The absorption process expresses itself in the time-domain signals as a decrease in amplitude and an associated phase shift of the observed THz pulse. The temporal electric field created from a THz-TDS spectrometer is depicted in Figure 2.1, where the black curve represents the reference signal collected without any sample present and the red curve represents the transmitted signal passing through the sample. The sample's complex permittivity and refractive index under examination can be determined by comparing the THz waveforms obtained with and without the sample.

Van Exter et al. conducted one of the first THz-TDS experiments in 1989, which focused on examining THz pulse propagation through water vapor [33]. While there are several approaches for producing and detecting THz radiation, the use of photoconductive antennas, as reported in [33], was notable for its use of coherent detection, which allowed direct mapping of the THz field in time. Due to the rapid changing of the electromagnetic field, most electromagnetic detectors solely measure light intensity and cannot resolve electromagnetic field oscillations in time. THz-TDS achieves coherent detection by employing an ultrashort laser with durations of the order of 100 femtoseconds for both THz pulse production and detection. The ultrashort pulse is divided into two segments: one generates the THz pulse, while the other gates the detector and arrives simultaneously with the THz pulse at the detector. When the gate pulse reaches the detector, it causes

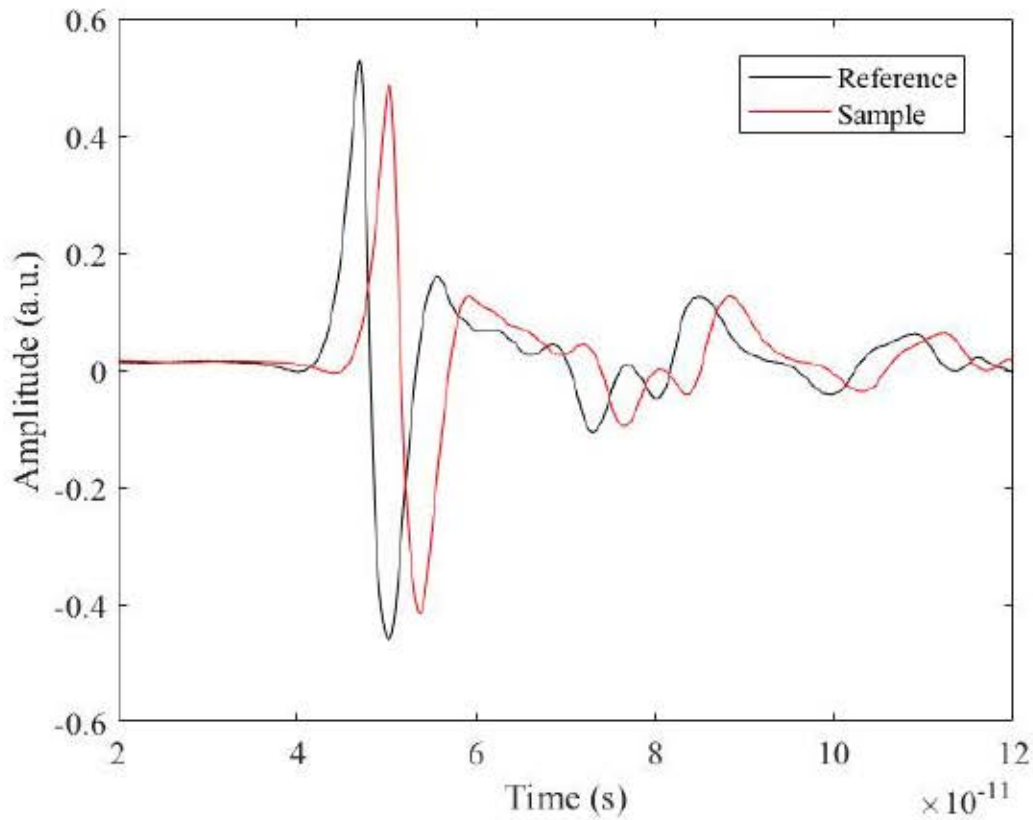


Figure 2.1: THz time-domain signals with and without using a 4.4 mm thick oven-dried microcrystalline powder in a petri dish. This Figure clearly indicates the change in amplitude (lower amplitude for sample waveform as compared to reference due to radiation absorption by cellulose powder) and a phase shift (waveform comes later in time (a time delay) due to the slower propagation speed of radiation in the cellulose powder as compared to air).

a current proportional to the THz pulse's electric field, allowing for coherent detection. The field is mapped out in time by varying the optical delay between the gating optical pulse and the THz pulse being detected. The experimental setup for THz-TDS spectroscopy is depicted in Figure 2.2, and the section that follows will describe the physical principles underpinning generation and detection.

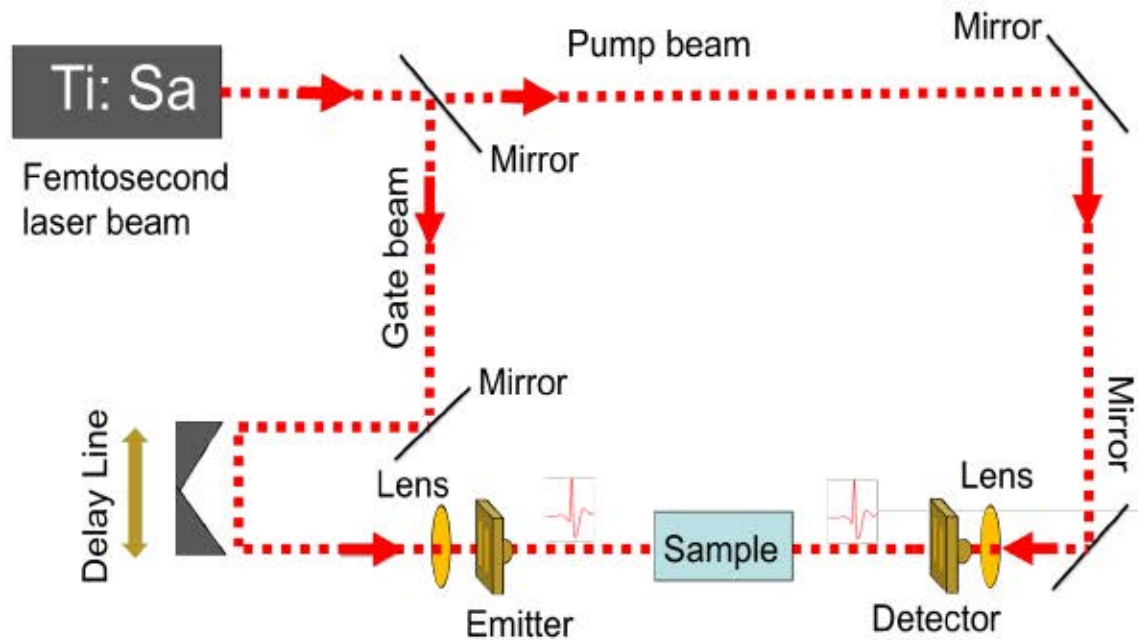


Figure 2.2: The experimental setup of THz-TDS. The femtosecond (fs) laser beam output is divided into two parts with the help of a beam splitter. One part of the beam is used to generate the THz radiation, and the other half is passed through the delay line and used to detect the THz beam. The probe beam gates the photoconductive detector, which overlaps the created THz pulse. The field is mapped out in time by varying the optical delay between the gating optical pulse and the THz pulse being detected.

2.2 THz radiation emission

Auston et al. first demonstrated pulsed THz radiation production and detection using photoconductive antennas in 1984 [34]. There are two main methods for producing pulsed THz radiation: Nonlinear optical approaches [35] and Photoconductive antennas [34] [35]. The Photoconductive antennas were used exclusively in this thesis to generate and detect THz radiation, and the basic principles of operation are explained for this configuration next.

2.2.1 Generation of THz using photoconductive antennas

To begin this process, an ultrashort fs laser generating pulses of roughly ~ 100 fs is focused onto a biased antenna located on a semiconductor substrate. Laser photons have an energy that exceeds the band gap, resulting in the generation of a transitory photocurrent. This brief photocurrent is caused by photocarrier acceleration in the externally applied biased electric field. According to Maxwell's equations, this transient photocurrent emits THz radiation with wavelengths in the THz region [35]. The THz electric field, E_{THz} , is directly proportional to the temporal derivative of the transient photocurrent density, dj/dt , produced in the transmitting antenna.

Various optical wavelengths can be used for the excitations, and depending on the optical wavelength used for the excitation, THz radiation can be created by a photoconductive antenna made of different materials, such as gallium arsenide (GaAs) and InGaAs. Most THz systems use a substrate with a short carrier lifetime in the sub-picosecond region to make the most of ultrafast laser excitation to produce a transient photocurrent that is as short as possible. As a result, low-temperature (LT) GaAs is often used, which has a carrier lifetime of less than a picosecond, over conventional GaAs, which has a carrier lifetime of several hundred picoseconds [36]. The goal is to create a very short $j(t)$, so that dj/dt is as large as possible.

The process of generating THz electromagnetic radiation starts when a fs laser pulse having intensity $I(t)$ excites a biased semiconductor with photon energies greater than its bandgap. This begins the production of electrons and holes in the conduction and valence bands, respectively, and the rapid change of the transport photocurrent gives rise to electromagnetic radiation. The equation for photocurrent (J) can be written as [37]

$$J = env, \quad (2.1)$$

where e is carrier charge, v is carrier speed, and n is the carrier density. The change in photocurrent (J) can arise from two processes. The first is from the acceleration of carriers under the influence of an electric field, $en\frac{\partial v}{\partial t}$ and the second is due to the rapid change of the carrier density via a fs laser pulse, $ev\frac{\partial n}{\partial t}$. Thus, according to the origin of electromagnetic radiation from a biased semiconductor, it can be divided into two parts (refer to equation 2.2): the first part is due to carrier acceleration and the second is due to change in carrier density.

$$E_{\text{THz}} \propto ev\frac{\partial n}{\partial t} + en\frac{\partial v}{\partial t}. \quad (2.2)$$

2.3 Detection of THz using photoconductive sampling

THz detection by photoconductive sampling is identical to photoconductive generation, except for how the bias electric field is provided to the antenna. The bias electric field is provided by the electric field of the focused THz pulse directed onto the antenna. An ultrashort fs laser is utilized to illuminate the $\sim 5 \mu\text{m}$ gap between the electrodes on the semiconductor surface, utilizing photons with energy larger than the band gap, forming a transient conductivity window. Throughout the lifespan of the transient conductivity window, the THz field generates a current proportional to its amplitude [19]. A lock-in amplifier, which works at the same frequency as the modulation of the emitter bias, amplifies and detects this current.

$$J(t) = \int_{-\infty}^t \sigma_s(t-t')E_{\text{THz}}(t')dt', \quad (2.3)$$

where $\sigma_s(t)$ is the transient surface conductivity [38]. The increased current results from a convolution of the THz field and the transient photoconductivity window.

2.4 Using THz radiation to probe samples

THz-TDS is typically performed either in transmission or reflection. Transmission geometry is particularly desirable for many applications, and it is the geometry employed in this study, which is explained in further detail in the next section. The emitter and detector were positioned in a line in the transmission configuration. A sample holder on a rotating mount was inserted between the transmitter and detector. This holder allows the sample to be placed at any angle. Typically, an aperture or lens is employed to limit the beam to only pass through the sample. The following procedure is used to perform measurements in the transmission geometry: (a) a reference scan is taken with no sample between the transmitter and receiver; (b) a sample scan is taken by adding a sample between the transmitter and receiver. The arrangement of the transmission configuration setup is shown in Figure 2.3. In this thesis, a modified Picometrix T-ray 4000 system was used to perform the THz-TDS. The T-Ray 4000 spectrometer generates THz signals at a rate of 1000 waveforms per second in an 80 ps window with a bandwidth from approximately 0.1-1 THz, and a THz beam diameter ($1/e$ electric field) of approximately 30 mm. The sample-specific details for the Picometrix T-ray 4000 system are discussed later in Chapter 4 by using MCC as a sample.

2.5 Analysis of the data

This section explores the mathematical methods for extracting information from acquired data in further detail. As discussed above, the transmission geometry is

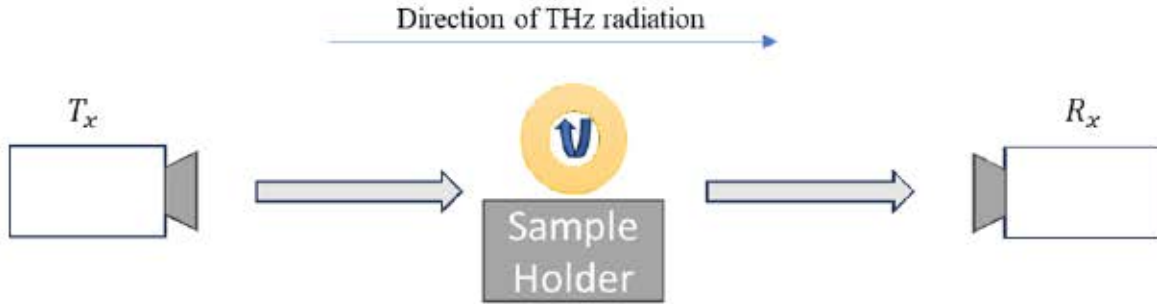


Figure 2.3: The configuration for transmission spectroscopy: T_x represents a transmitter and R_x represents a receiver.

used to acquire experimental data. The index of refraction and absorption coefficient are analyzed with the help of the MATLAB computer language. There are two models that were considered to analyze the data. The thick sample approximation of Duvillaret [39] and a fully numerical method (the inverse electromagnetic problem) developed by Koch et al. [40].

2.5.1 Duvillaret's Method

Duvillaret's method is computationally very fast for extracting the parameters of an optically thick material. The optically thick sample can be defined as a sample with temporally well-separated echoes of the THz pulse [39]. These echoes are caused by the multiple reflections within the sample. Thus, for optically thick samples, the first pulse that is directly transmitted through the sample is the main pulse, and its replicas can be ignored. This makes the case of optically thick samples easy to solve. It considers the following assumptions: The sample is homogeneous and has two flat and parallel sides. It also considers the magnetically isotropic nature of the sample, the neighboring materials, and the linear electromagnetic response of the media. One of the most critical parameters in this method is the thickness of the sample. According to this method, the complex dielectric function is calculated from the THz measurements by using the following rela-

tion [39] [41]:

$$\frac{E_B(\nu)}{E_A(\nu)} = \hat{t}_{AB}\hat{t}_{BA}e^{i\frac{2\pi\nu L}{c}(\hat{n}_b - \hat{n}_a)}, \quad (2.4)$$

where $E_A(\nu)$ is the electric field amplitude of the reference measurement $E_B(\nu)$ is the electric field amplitude of the transmitted field, ν is the frequency, L is the thickness of the sample under consideration, c is the speed of the light, \hat{n}_b is the refractive index of the sample, and \hat{n}_a is the refractive index of the reference. Also, \hat{t}_{AB} and \hat{t}_{BA} are the two Fresnel transmission coefficients from sample A to B and sample B to A, respectively. For normal incidence, the Fresnel transmission coefficients are given by:

$$\hat{t}_{ij} = \frac{2n_i}{n_i + n_j}, \quad (2.5)$$

where \hat{n}_i is the index of refraction of the incident medium and \hat{n}_j is the index of refraction of the sample. Also, the index of refraction may be complex in nature, so it can be defined as:

$$\hat{n}_b = n_b + ik_b \quad (2.6)$$

where n_b and k_b are the refractive index and extinction coefficient of the sample, respectively. The index of refraction and absorption coefficient can be calculated by using the following equations [39]:

$$n_b = -\frac{\theta c}{2\pi\nu L} + 1; \quad (2.7)$$

$$\alpha_b = -\frac{2}{L} \ln \left[\frac{R(n_b + 1)^2}{4n_b} \right], \quad (2.8)$$

where

$$\alpha_b = \frac{4\pi\nu k_b}{c}, \quad (2.9)$$

and R and θ are the amplitude and phase of the ratio of the reference field to the transmitted field when we compare it to the following equation in Euler form:

$$\frac{E_{\text{trans}}(\nu)}{E_{\text{ref}}(\nu)} = R e^{i\theta}, \quad (2.10)$$

where $E_{\text{ref}}(\nu)$ is the reference field in the frequency domain and $E_{\text{trans}}(\nu)$ is the transmitted field in the frequency domain. The frequency domain fields are obtained by Fourier transformation of the measured time-domain signals.

To highlight the thick sample approximation method, 20 sheets of paper are used as the sample, from which the index of refraction and absorption coefficient can be determined. Each sheet of paper is approximately 0.1 mm thick. The data was collected using the modified Picometrix T-Ray 4000 THz spectrometer as described in section 2.4 at the Wood Innovation Research Lab (WIRL). The THz signals of the 20 sheets of paper with and without samples can be found in Figure 2.4.

The results of paper spectroscopy using Duvillaret's method of analysis are given in Figures 2.5 and 2.6. These two Figures indicate the variation of the mean value (red line in Figures 2.5 and 2.6) of the index of refraction and absorption coefficient with respect to frequency, obtained by using the THz data from five different runs and averaging them. The black lines in Figures 2.5 and 2.6 indicate the one standard deviation error bars for an index of refraction and the absorption coefficient, respectively. As indicated from Figure 2.5, the refractive index of the paper is almost constant with frequency, and the absorption coefficient, Figure 2.6, of the paper increases with increasing frequency. As the error bars in both Figures 2.5 and 2.6 are relatively narrow, this indicates most of the data for paper spec-

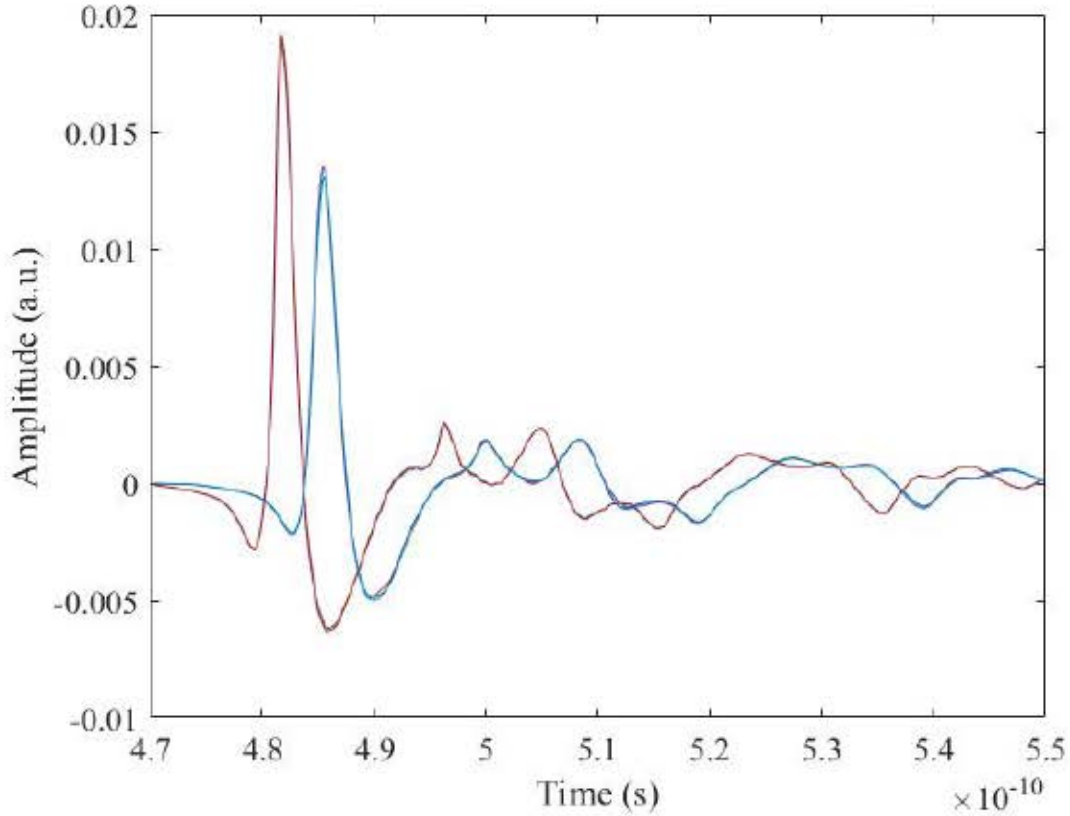


Figure 2.4: Variation of the amplitude of the THz beam in the presence and absence of sample with respect to time for paper. Red line: reference THz beam, and blue line: beam in the presence of the sample.

troscopy obtained using THz-TDS is placed around the mean value and there is low variability and error in the measurements.

Because the thickness of the sample is known, the index of refraction and absorption coefficient can also be calculated by using the explicit relations given below:

$$n = n_{\text{air}} + \frac{c_0 \cdot t_{\text{delay}}}{d}; \quad (2.11)$$

$$\alpha = -\frac{2}{d} \log \left(\frac{E_{\text{sample}}}{E_{\text{reference}}} \right), \quad (2.12)$$

where n_{air} stands for the index of refraction of air, c_0 is the speed of light, t_{delay}

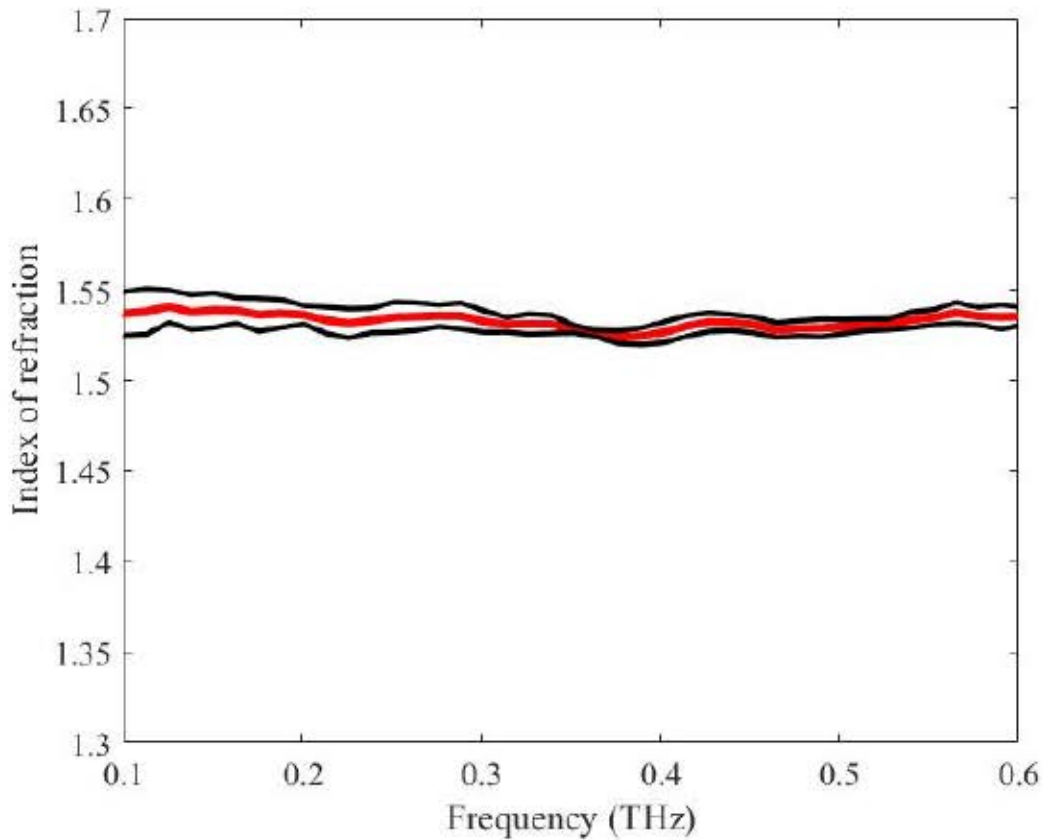


Figure 2.5: Variation of Index of refraction with respect to frequency by calculating the mean (red) and standard deviation (black) for five runs for 20 sheets of paper as a sample.

is the time delay between the reference signal and the sample signal, and d is the thickness of the sample. Also, E_{sample} indicates the field when the THz beam passes through the sample, and $E_{reference}$ is the field when no sample is in place. The time delay between the reference and sample THz waveforms (3.9 ps) from Figure 2.4 and the known thickness of the sample (2 mm) is used to calculate the index of refraction explicitly by using equation 2.11, which came out to be 1.58, which is comparable with the value of the index of refraction, 1.54, found in Figure 2.5 with a percentage difference of 2.5%. Similarly, the absorption coefficient for the sample can be explicitly derived by using equation 2.12 and the change in amplitude between the sample and reference THz waveform in Figure 2.4. By us-

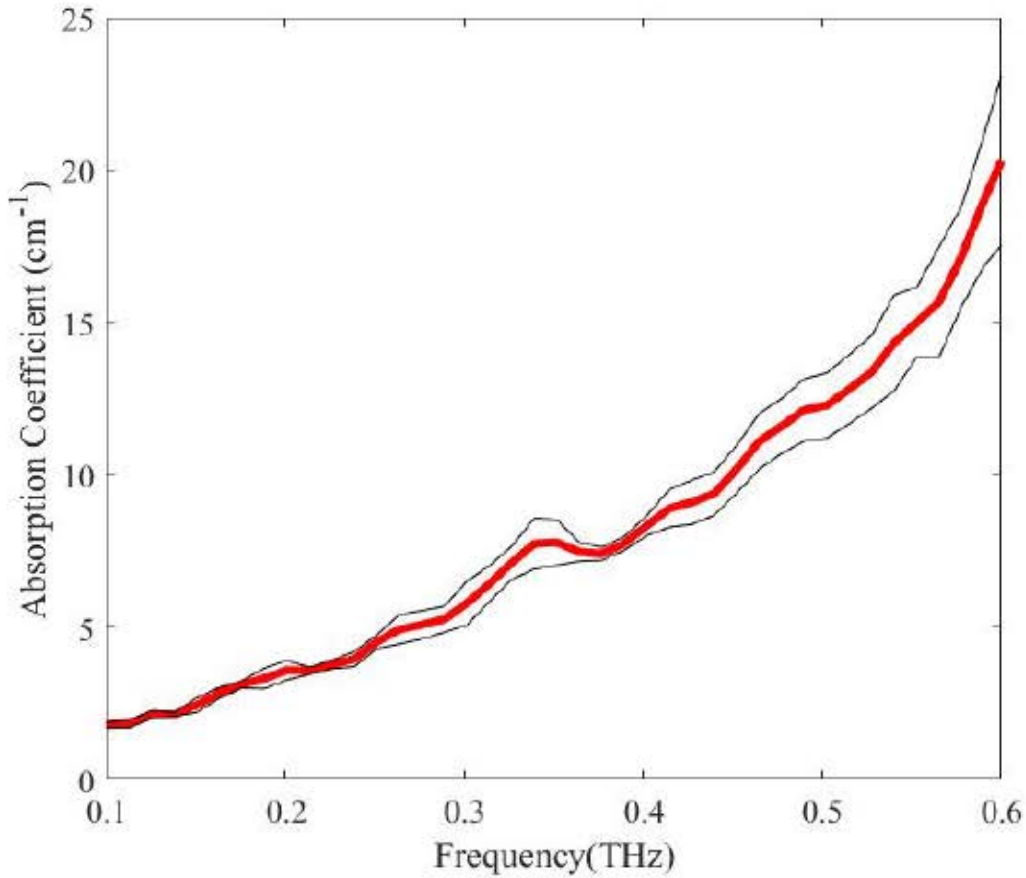


Figure 2.6: Variation of absorption coefficient with change in frequency by calculation mean and standard deviation for five runs for 20 sheets of paper as a sample.

ing the thickness, d , as 2 mm and the ratio of sample to reference amplitude (refer to Figure 2.4), it came out to be approximately 1.62 cm^{-1} . This is consistent with the results found in Figure 2.6, as the absorption coefficient started varying from 1.59 to 20.06 cm^{-1} , with frequency ranging from 0.1 to 0.6 THz.

2.5.2 The Numerical Method

The second method is called the inverse electromagnetic problem because, in this method, the refractive index is measured by the effect caused on the electric field of a THz wave after passing through the material under study, as given in Koch et al. [40]. Like the previous method, it makes some assumptions and uses a specific

notation to describe the method mathematically. In this method, it is assumed that the properties of the materials are homogeneous with respect to position and direction. The second important assumption is that the interfaces between the mediums are flat and parallel to each other, thus neglecting any scattering of the beam. This method also assumes the normal incidence of THz radiation so that the angle of incidence is zero.

As the ray is reflected and transmitted multiple times, for the material parameter extraction, the first step is to perform the preliminary signal processing, which includes the linear offset compensation of raw time domain data and the determination of the reliable frequency range. Moreover, this method is useful for evaluating the unknown sample's thickness. This can be done by first considering the appropriate thickness range and then by determining the degree of total variation (TV) from the index of refraction and absorption data. Therefore, another difference between the two methods discussed is that Koch's method can be used for highly dispersive and noisy data. This method works on the condition that the waveforms contained in the time-domain data should have one main transmission and at least two smaller multiple reflections. These two smaller reflections are obtained due to the multiple internal reflections in the sample, which is expected, i.e., the Fabry-Perot effect.

Assuming that $E_{ref}^{ex}(\omega)$ and $E_{trans}^{ex}(\omega)$ are the reference and transmitted signals, then the equation for the frequency-dependent transfer function can be written as [40]

$$H_{\text{experiment}}(\omega) = \frac{E_{\text{trans}}^{ex}(\omega)}{E_{\text{ref}}^{ex}(\omega)} \quad (2.13)$$

The signal propagation through the sample is shown in Figure 2.7. The 0 and 1 written at the top of Figure 2.7 indicate air and sample, respectively.

As indicated in Figure 2.7, when the electric field approaches the flat or par-

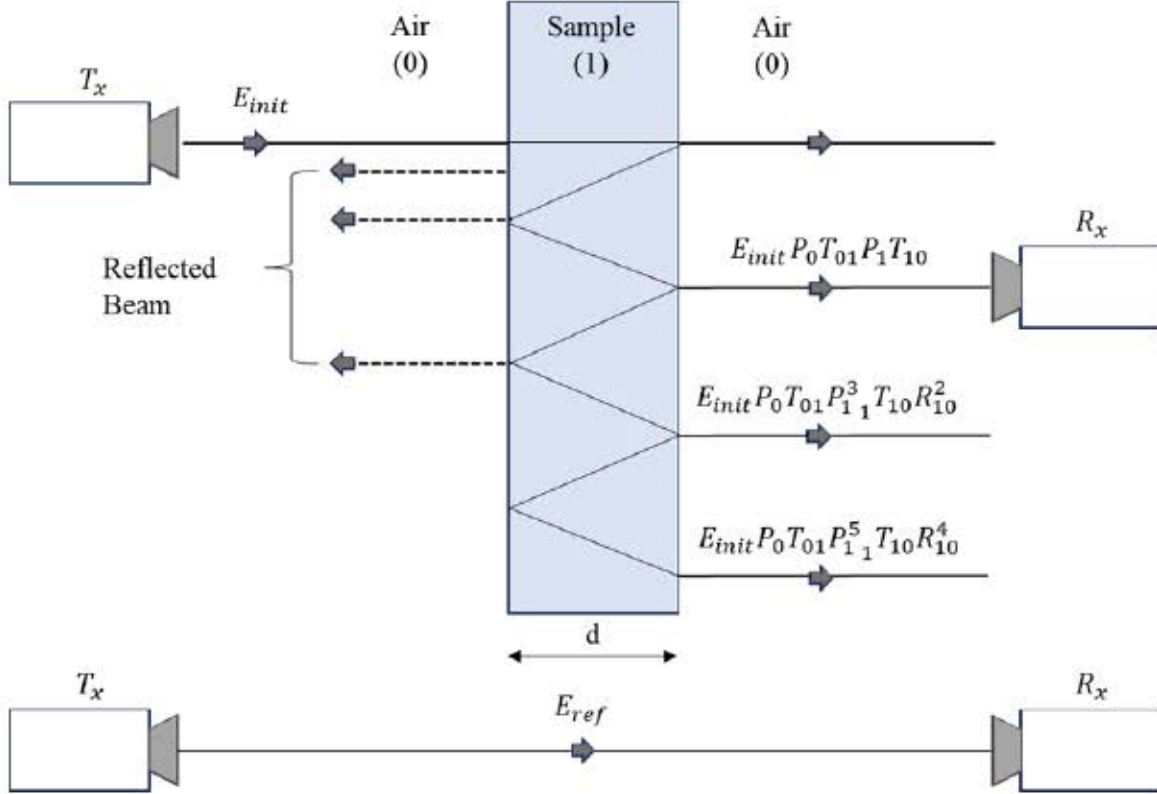


Figure 2.7: The representation of Fabry-Perot reflections from the incident electric field E_{init} transmitting through the sample with a different refractive index that is surrounded by air. T_x represents a transmitter and R_x represents a receiver.

allel edges, it gets divided into two portions. One portion is the reflected part of the initial electric field, and the remaining portion gets transmitted into the sample. Then, the transmitted portion in the sample experiences multiple internal reflections in the sample and these reflections are known as Fabry-Perot reflections. With each consecutive reflection, the intensity of the electric field gets weaker. In transmission spectroscopy, the reflected signal is not a part of E_{trans} , therefore it is neglected. Therefore, after collecting all the multiple reflections from this geometry, the equation for E_{trans} can be written as,

$$E_{trans} = E_{init} P_0(x-l) t_{01} P_1(l) t_{10} \left[1 + \sum_{i=1}^{\delta} (r_{10}^2 P_1^2)^i \right], \quad (2.14)$$

where δ represents the number of Fabry Perot reflections, l indicates the thickness

of the sample, r_{01} is the Fresnel reflection coefficient from air to sample and, t_{01} indicates the Fresnel transmission coefficient from air to sample that can be calculated using equation 2.5. The expression for the reference THz field that only propagates through air can be written as:

$$E_{\text{ref}} = E_{\text{init}} P_0(x) \quad (2.15)$$

Therefore, the expression for the theoretical transfer function for which the ratio of E_{trans} to E_{ref} can be written as:

$$H_{\text{theo}} = \frac{E_{\text{trans}}}{E_{\text{ref}}} = P_0(-l) t_{01} P_1 t_{10} \left[1 + \sum_{i=1}^{\delta} (r_{10}^2 P_1^2)^i \right] \quad (2.16)$$

This transfer function can be used to obtain the material parameters, the index of refraction (n), and the extinction coefficient (k), which can be extracted numerically. To extract these parameters, first the assumption of the range of n and k is made. The best combination is taken where H_{theo} is arbitrarily close to H_{exp} . To achieve the proper convergence of the results, the number of Fabry Perot reflections is also assumed. This can be done as follows:

$$E_{\text{trans,max}} = E_{\text{ref,max}} \cdot \exp\left(-\frac{\omega}{c_0} k_1 l\right), \quad (2.17)$$

therefore, k_1 becomes:

$$k_1 = -\frac{1}{l} \cdot \frac{c_0}{\omega} \cdot \log\left(\frac{|E_{\text{trans,max}}|}{|E_{\text{ref,max}}|}\right). \quad (2.18)$$

Here, $E_{(\text{ref,max})}$ and $E_{(\text{trans,max})}$ represent the maximum reference and transmitted signal respectively.

$$\Delta t = \frac{l \Delta n}{c_0}, \quad (2.19)$$

$$n_1 = \frac{c_0 \Delta t}{l} + n_0, \quad (2.20)$$

where, δt is the time delay between two signals and δn is the difference between the index of refraction for sample and air, c_0 is the speed of light and the thickness of the sample is indicated by l . Also, for this method, the number of Fabry-Perot reflections, indicated by δ , should be the greatest integer that satisfies the following relation:

$$t_{\max} \geq \frac{n_1}{c_0} l (1 + 2\delta), \quad (2.21)$$

It is important to note that this method can only be implemented when the samples are thin (when compared to optically thick samples, multiple reflections need to be present in the measured signal) and they experience multiple reflections that fall within the temporal window of the accumulated THz signal. The analysis using this method was performed on the same sample that was used in Duvillaret's method, i.e., 20 sheets of paper, with each sheet of paper approximately 0.1 mm thick. The same sample was taken to make a comparison between the results obtained with both methods. The data was collected using a modified Picometrix T-Ray 4000 THz spectrometer (refer to section 2.4 for details) present at the Wood Innovation Research Lab (WIRL). The results for an index of refraction and an absorption coefficient are presented in Figures 2.8 and 2.9, respectively. From the comparison of the index of refraction (Figure 2.5) and absorption coefficient (Figure 2.6) obtained by Duvillaret's method to the index of refraction (Figure 2.8) and absorption coefficient (Figure 2.9) obtained with the numerical method, the results for the index of refraction came out to be comparable to each other with a percentage difference of 2.63%.

In this thesis, we will mostly use Duvillaret's method to analyze because the

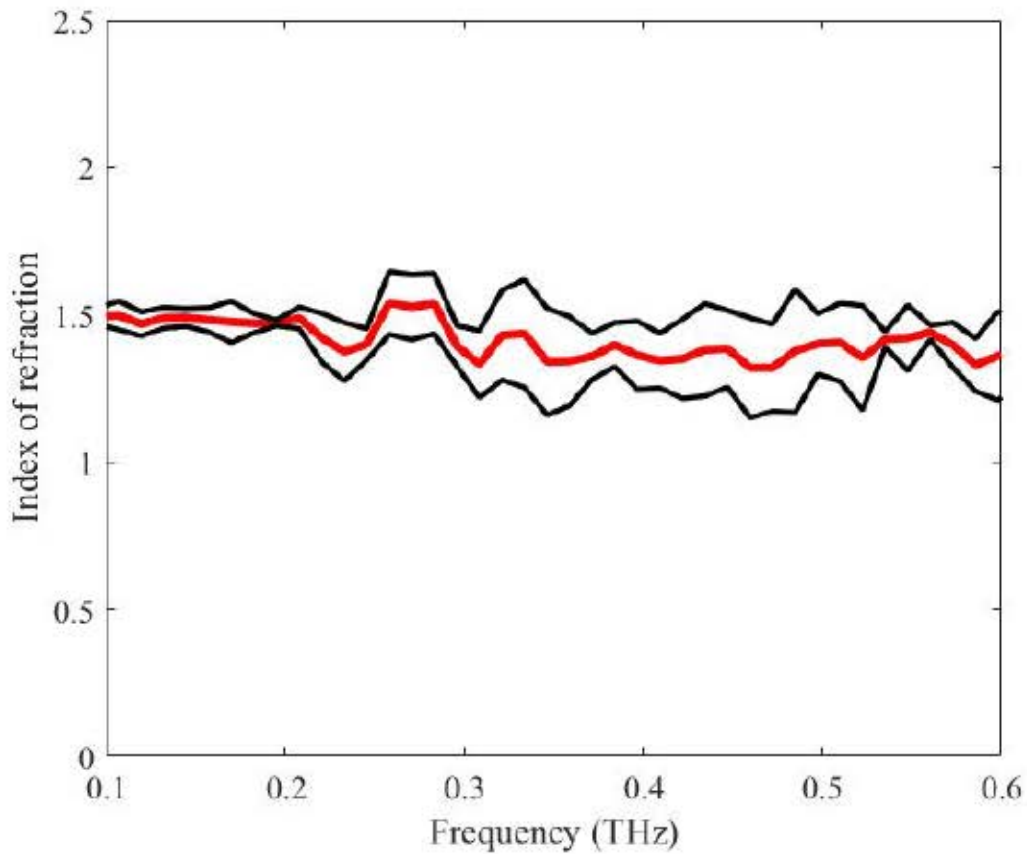


Figure 2.8: Index of refraction for 20 sheets of paper as a sample using Koch's method.

thickness of the material gives no multiple reflections in the temporal window, although the numerical approach within the numerical method will also be used to analyze data later in the thesis.

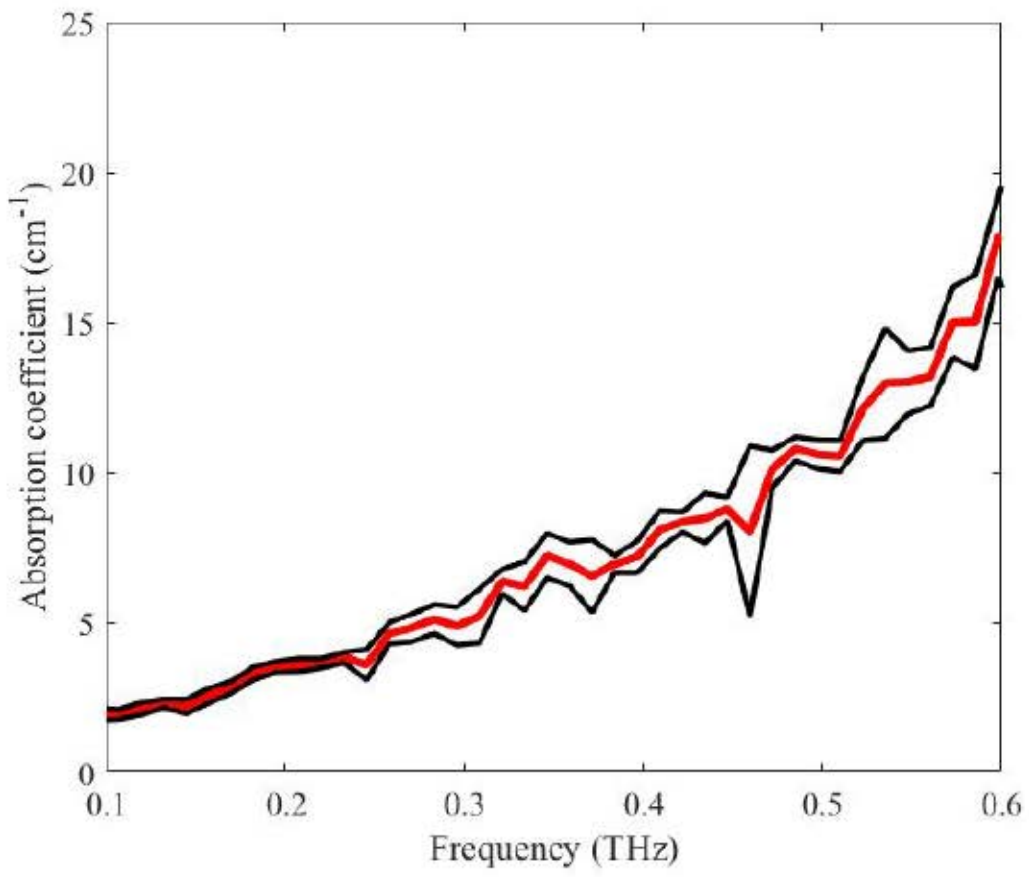


Figure 2.9: Absorption coefficient for 20 sheets of paper as a sample using Koch's method.

Chapter 3

Microcrystalline Cellulose: Structure and Interaction with Water

3.1 Abstract

The hydration of microcrystalline cellulose (MCC) with water vapor sorption using Brunauer-Emmett-Teller (BET) theory was studied. From the sorption isotherm, it was found that there may be different kinds of water present during the hydration of microcrystalline cellulose as the relative humidity (RH) increases. The specific surface area was calculated using Brunauer-Emmett-Teller (BET) nitrogen adsorption, and it came out that the specific surface area of MCC is much larger when it is calculated using water adsorption. Thermogravimetric analysis (TGA) was performed to understand the thermal properties of microcrystalline cellulose.

3.2 Introduction

In wood science, extensive research has been dedicated to understanding the interaction between water and wood material, often employing techniques like THz-

TDS. However, to understand water-wood interactions comprehensively, exploring how water behaves within wood composites, especially cellulose, is essential. This study is important to understand whether the overall behavior of MCC remains consistent with that of wood or exhibits variations.

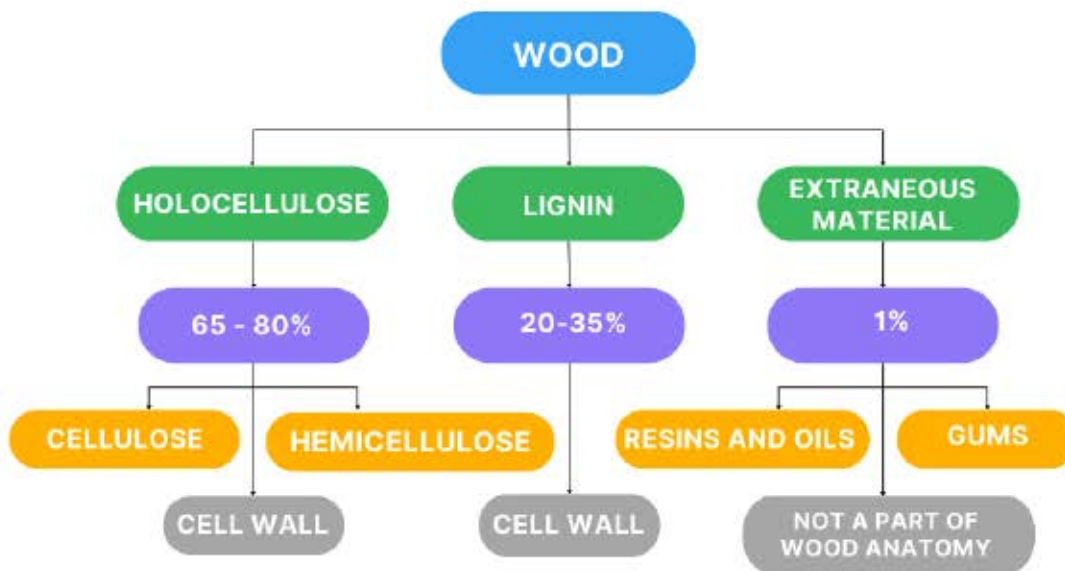


Figure 3.1: Flowchart of the chemical composition of wood.

Wood, a complex and natural material, primarily comprises three fundamental constituents: holocellulose, lignin, and extraneous matter. Holocellulose, constituting approximately 65-80% of wood's composition, encompasses cellulose and hemicellulose. However, it is crucial to recognize that the exact proportions of these constituents can exhibit considerable variation based on the wood species or even variations within the same species. In addition to holocellulose and lignin, wood contains extraneous materials, such as organic extractives and inorganic

minerals. The elemental composition of wood primarily consists of 50% carbon, 6% hydrogen, and 44% oxygen. Trace amounts of various metal ions are present in wood, contributing to its overall chemical composition [42]. The flowchart illustrating the chemical composition of wood is given in Figure 3.1. Given that cellulose is the primary component of wood, this thesis focuses on using MCC as a model material to study water's interaction and behavior. Using MCC offers several advantages, primarily eliminating various extraneous materials present in natural wood, thereby simplifying the study model. Furthermore, MCC's well-defined crystalline structure facilitates precise investigations into water-cellulose interactions.

The study of water interaction with MCC is an important step in understanding fundamental processes relevant to wood science and industrial applications of wood science using THz spectroscopy. Therefore, the upcoming paragraphs will discuss the details of cellulose and MCC and finally discuss the interaction of water with cellulose.

Cellulose, the predominant component of plant cell walls, accounts for approximately 40-45% of their composition. It is a linear polymer composed of β -D glucose units [43], linked by (1 \rightarrow 4) glycosidic bonds to form cellobiose residues, the repeating units within the cellulose chain. The chemical constitution of cellulose is represented in Figure 3.2. The β configuration induces a 180° rotation of alternating glucose units, making the cellulose chains rigid and straight. The inherent stiffness and linearity of cellulose chains favor their organization into bundles with a high degree of crystalline order, stabilized by hydrogen bonds. Depending on the different plant tissues, the proportion of cellulose in them varies. As an example: wood contains approximately 40-50% of cellulose on an oven-dry basis, as discussed earlier, and there is approximately 98% cellulose present in cotton hair. To study the interaction of water with cellulose (our purpose), it is important

to consider that cellulose possesses highly ordered crystalline regions, it also contains disordered or amorphous regions. Cellulose is insoluble in water due to the robust hydrogen bonding between its chains, preventing water from disrupting these bonds. However, cellulose readily absorbs and desorbs water in the amorphous regions where hydroxyl groups are not engaged in interchain bonding.

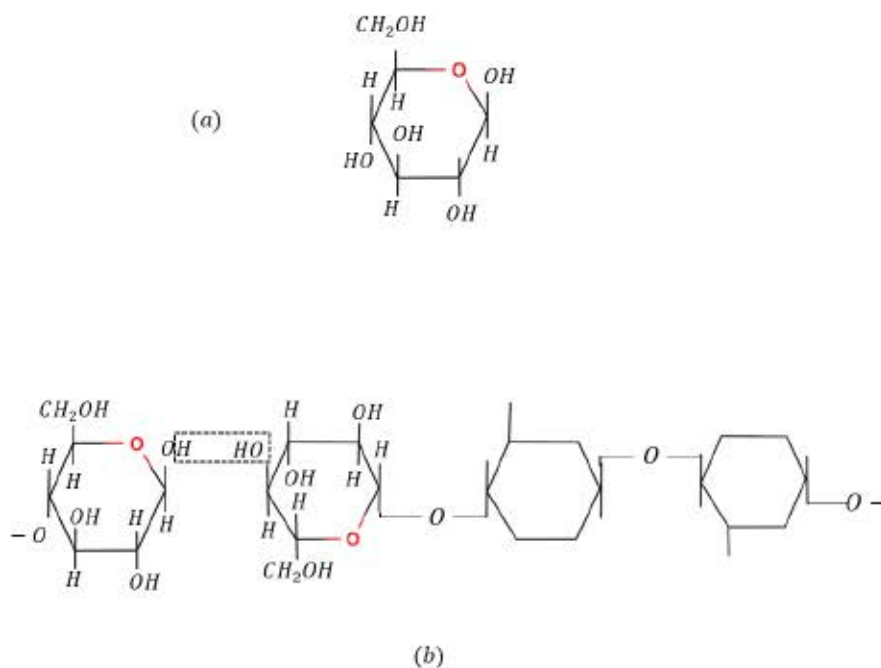


Figure 3.2: The chemical constitution of cellulose. (a) Molecule of β -glucose (b) representation of part of the cellulose molecule, a 1-4 polymer of β -glucose.

MCC, a naturally occurring substance is obtained from purified and partially depolymerized cellulose [44]. Its purification process of the treatment of α -cellulose with an excessive amount of mineral acids, among other important steps [44] [45] [46]. Marketed by FMC Corporation, MCC was first commercialized in 1962 under the name Avicel[®].

MCC can either be obtained in a fine-particle powdered form or a colloidal form. Figure 3.3, describes the manufacturing process of MCC from the cellulose sources. In recent times, MCC has garnered significant industrial attention

due to its versatile applications, including its use as a raw material in the production of synthetic yarn and its relevance in pharmacology, cosmetics, and ceramics [45] [47]. The applications of MCC can be modified according to their resultant form. For example, if present in colloidal form, MCC can be used as a suspension stabilizer, a water retainer, a viscosity regulator, and an emulsifier in different pastes and creams. In powder form, it can be used as a binder and filler in food, medical tablets, and particularly as a reinforcement agent [48] in the development of polymer composites.

MCC is known for its stiffness, strength, fibrous nature, non-toxicity, water insolubility, crystallinity, cost-effectiveness, low density, biodegradability, and renewability, making it an attractive choice in various applications in different fields [49].

THz-TDS has gained a lot of interest in studying cellulose. In one of the cases, the crystallinity index of MCC was studied by combining the THz-TDS with the partial least square method [24]. In another case, the THz-TDS was used to perform the crystallographic analysis in cellulose obtained from different sources [22]. THz-TDS has been used to study the artifacts made up of cellulose and provide a quantitative assessment of the state of preservation of those artifacts [14] [26]. It has been used to measure the effective refractive index and absorbance spectra of whole tablets made up of MCC and other components and to quantify fragmentation upon tableting [25].

In this thesis, we will be using THz-TDS to probe water dynamics in MCC. To probe water dynamics in the cellulose structure, it is first important to study the sorption isotherm of the MCC. To study the sorption isotherms, we are first going to define the MC in the next paragraph.

Most natural materials are inherently hygroscopic, which means that their MC varies in response to changes in RH and temperature (T) in their surroundings.

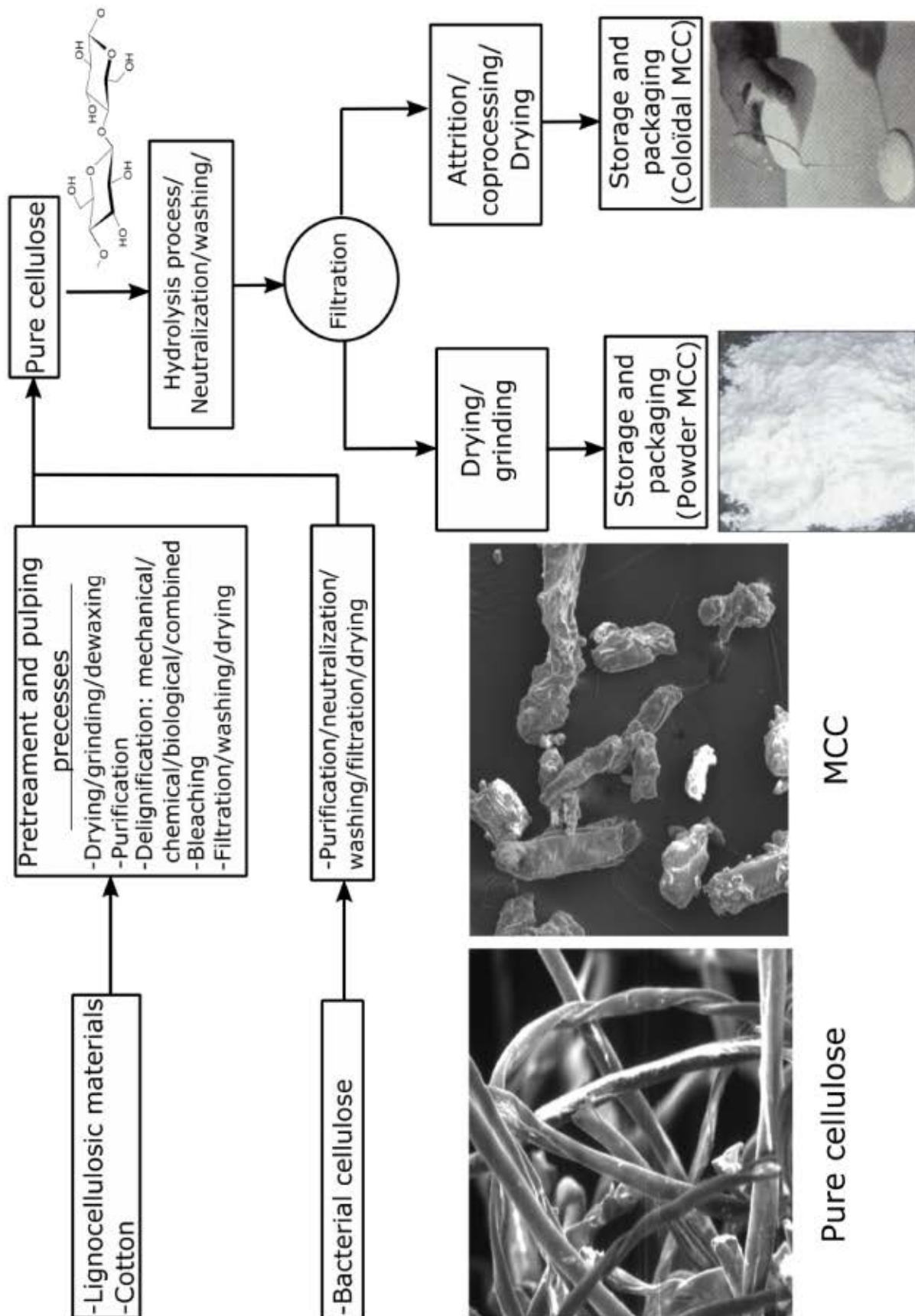


Figure 3.3: The manufacturing process of MCC from the cellulose sources. As adapted from: Trache et al. 2016

With the change in MC, the physical and mechanical properties of materials change [50] [51]. In this study, MC is assessed on an oven-dry basis, expressed as a percentage difference between the wet mass and the mass obtained after oven-drying. [32]:

$$MC = \left(\frac{m - m_{od}}{m_{od}} \right) \times 100\% \quad (3.1)$$

where, m represents the wet mass, and m_{od} is the mass after oven-drying. The following paragraphs are going to discuss the important details of sorption isotherms and water sorption in cellulose.

When a hygroscopic material is exposed to a fixed RH at a constant temperature, the material develops the same MC as the surrounding atmosphere, which is known as the equilibrium moisture content (EMC). The relationship between EMC and RH is often depicted as a sorption isotherm. These isotherms vary significantly depending on the material under examination, making them valuable tools for probing the interaction of water with samples. Therefore, these sorption isotherms can be described as the variation of the mass of water taken up per unit mass of dry solid versus RH, $100(P/P_0)$, where P and P_0 are the water vapor pressure and the pressure of the pure liquid water, respectively. A typical sorption isotherm for MCC, studied using the physical adsorption of gases, has been characterized by its classical sigmoid shape [52]. This sigmoid shape of the isotherms suggests the classical models and equations that can be used to describe the physical adsorption of gases. These models are often referred to as sorption models. These theories describe how sorbing molecules like water interact with the adsorption surface.

In this thesis, we used the BET theory named after the authors Brunauer, Emmett, and Teller to describe the sorption of water in cellulose. BET theory considers multilayer adsorption by designating the primary and secondary water molecules. In this multilayer adsorption theory, it is considered that the monolayers are tightly

bound to the cellulose and the secondary (or higher) layers behave more like liquid water [52] [53].

The BET equation, which can be used to describe the relationship between moisture content (M), RH fraction (h), moisture adsorbed by the monolayer (M_m), and a constant (C) is given as:

$$\frac{h}{M(1-h)} = \frac{1}{M_m C} + \frac{(C-1)h}{M_m C} \quad (3.2)$$

The equation of a line in general for a slope s and intercept i , can be presented as:

$$y = ms + i \quad (3.3)$$

When compared, equations 3.2 and 3.3 generate a straight-line relationship between $\frac{h}{M(1-h)}$ and the relative pressure (h). From comparison, the slope (s) and intercept (i) can be written as

$$s = \frac{C-1}{M_m C} \quad (3.4)$$

$$i = \frac{1}{M_m C} \quad (3.5)$$

By combining the equations 3.4 and 3.5, M_m can be obtained as

$$M_m = \frac{1}{s+i} \quad (3.6)$$

As a powerful tool for understanding moisture adsorption, the BET equation (equation 3.2) can be employed to construct BET isotherms.

The BET equation was modified to account for scenarios where multiple layers of water molecules may form on the surface. This modification allows for a more

comprehensive representation of moisture adsorption processes, considering the possibility of more water layers accumulating on the surface. The modified BET equation is given by:

$$M = M_m \frac{[Ch(1 - (n + 1)h^n + nh^{(n+1)})]}{(1 - h)[1 + (C - 1)h - Ch^{(n+1)}]} \quad (3.7)$$

where n is the number of layers and other variables have the same meaning as before.

As represented by equation 3.7, the modified BET equation can also be used to calculate the number of layers formed on the substrate (refer to Figure 3.5).

In the upcoming sections of this Chapter, the materials and methods used to study the sorption isotherm of MCC using BET theory will be discussed. Moreover, the BET theory was also used to determine the surface area available for nitrogen adsorption. TGA (Thermogravimetric Analysis) was performed on the MCC samples to study the thermal stability and water loss in MCC.

3.3 Materials and methods

The materials and methods used in study of this Chapter are discussed next.

3.3.1 Sorption isotherm

The MCC was obtained from Sigma-Aldrich, and at first, the MCC powder was oven-dried in a convection oven for 24 hours at $100 \pm 2^\circ\text{C}$ to determine the oven-dried mass of the MCC. Once the powder was oven-dried, approximately 15 (± 0.02) grams of MCC were weighed on the scale and transferred to a clear petri dish with 100 mm \times 15 mm dimensions. The powder was then settled with the help of vibrations for at least five minutes. Once the thickness of the powder was uniform, the pre-measurements of thickness and mass were taken. Afterward, the filled

petri dishes were conditioned at different RHs to obtain different MCs. This was done with the help of desiccators with constant RH and saturated salt solutions. The saturated salt solutions contained Lithium Chloride (LiCl, RH = 11.3%), Calcium Chloride (CaCl₂, RH = 31%), Potassium Fluoride (KF, RH = 65%), Sodium Sulphate (Na₂SO₄, RH = 91%), and water (H₂O, RH=99%) obtained from SIGMA-ALDRICH. The samples were left in the desiccators for at least 48 hours to make sure that they had an EMC. Once the equilibrium was reached (determined by no change in mass), the samples were removed from the desiccators, and the mass and thickness of the MCC were recorded again. This data collection was used to get the variation of MC in MCC with respect to RH, to produce sorption isotherm. The saturated salt solution and their corresponding RH used to study the water sorption in MCC are summarized in Table 3.1.

Saturated Salt Solution	Relative Humidity (RH%)
Lithium Chloride	11.3
Calcium Chloride	31
Potassium Fluoride	65
Sodium Sulphate	91
Water	99

Table 3.1: Saturated salt solutions and their corresponding RH% used to study moisture sorption by the MCC samples.

3.3.2 Nitrogen sorption

Using Brunaur-Emmett-Teller (BET) theory, [54] specific surface areas and the pore distribution of samples were measured using Autosorb-1 device Quantachrome instrument. The sample was outgassed at 105°C for 21 hours and measured for surface area and adsorption/desorption on a NOVA 2000e surface area analyzer.

3.3.3 Thermogravimetric Analysis (TGA)

Thermo-gravimetric analysis (TGA) was used to determine the thermal stability of MCC. It was performed on TA Instruments Discovery (TGA), from 25°C to 700°C, at a rate of 1°C/min and 10°C/min under a nitrogen flow rate of 25 mL/min.

3.4 Results and discussion

The sorption isotherm of MCC is depicted in Figure 3.4. It was noticed that moisture sorption in MCC is linear at RH levels below 25% as moisture uptake in MCC remains low and gradual within this RH range. However, as RH increases beyond this range, the MC in MCC rises more rapidly, signifying increased moisture adsorption and the relationship is not linear anymore. In fact, a deviation from linearity and an upward shift was observed in the region of about 65% RH. A similar trend was noticed by Stubberud et al. [55] in the study of sorption isotherms for MCC.

The sigmoidal shape of the isotherm was obtained by using equation 3.7, for the number of layers (n) is equal to 1 and 10, as represented in Figure 3.5. It was found that the BET equation does fit the water vapor sorption data of MCC, but only up to between 0.3 to 0.4 RHs, as consistent with Zografis et al. [52]. The value of W_m , which is the weight sorbed corresponding to one water molecule per sorption site on the solid, came out to be 0.052 g H₂O/g of dry MCC and may represent the amount of water absorbed in the monolayer.

These BET results can be explained with the help of a general model for water sorption on cellulose and starch by Zografis et al. [52] as follows: At low RH values, the water is bound directly to the available sorption sites in cellulose. Up to about 60% RH or at the intermediate values of RH, the polymer-polymer hydrogen bonds get broken, and this creates more primary sorption sites available for the upcoming

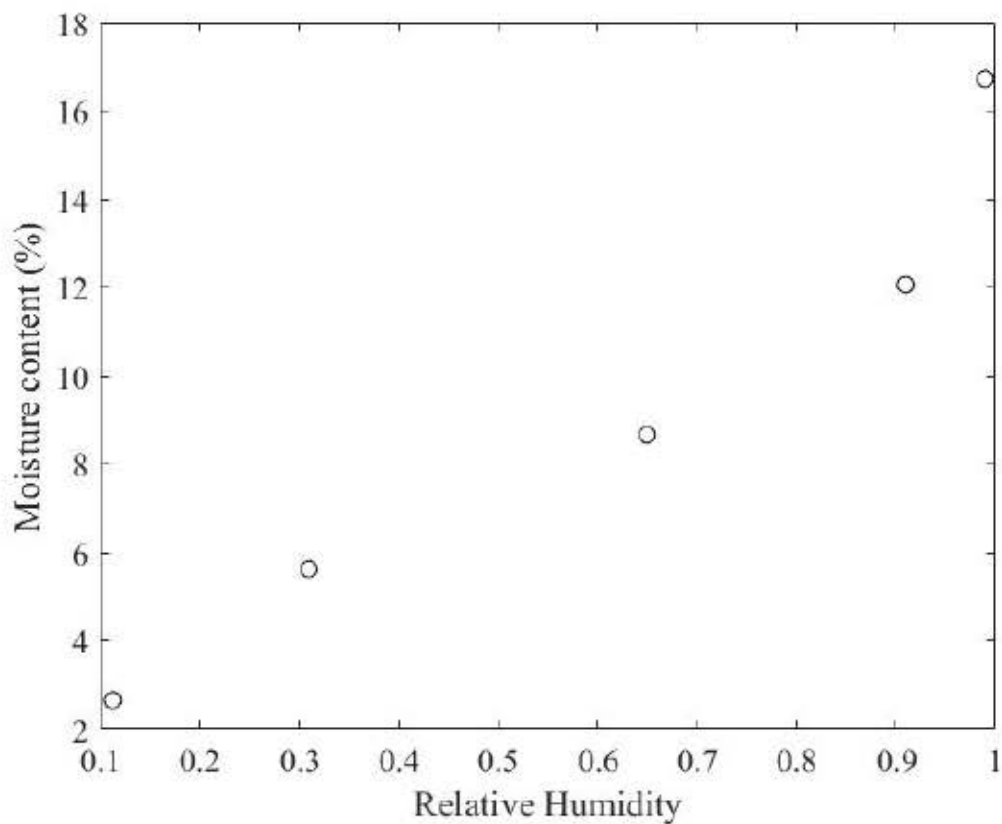


Figure 3.4: Variation of MC (oven-dry basis) in MCC as a function of RH.

water molecules. Thus, the water molecules start binding with the other water molecules already bound with the cellulose structure. In the end, with higher RHs, more sorption sites can become available and more water molecules can bind to the structure. At this point, the water may not bind directly to the sites that are bound to the primary sites, giving rise to different states of water. By using this model, we can interpret that the moisture below around 60% RH can reflect the properties of bound water, and at higher RH values, we can expect the water to behave like bulk water. This concept will be further studied in Chapter 4 of this thesis, but with the help of THz-TDS.

The BET-specific surface area using N_2 was $2.838 \text{ m}^2/\text{g}$ and the surface area available for water adsorption was calculated by the assumption that each water molecule occupies a surface area of 0.105 nm^2 , the surface area available for water

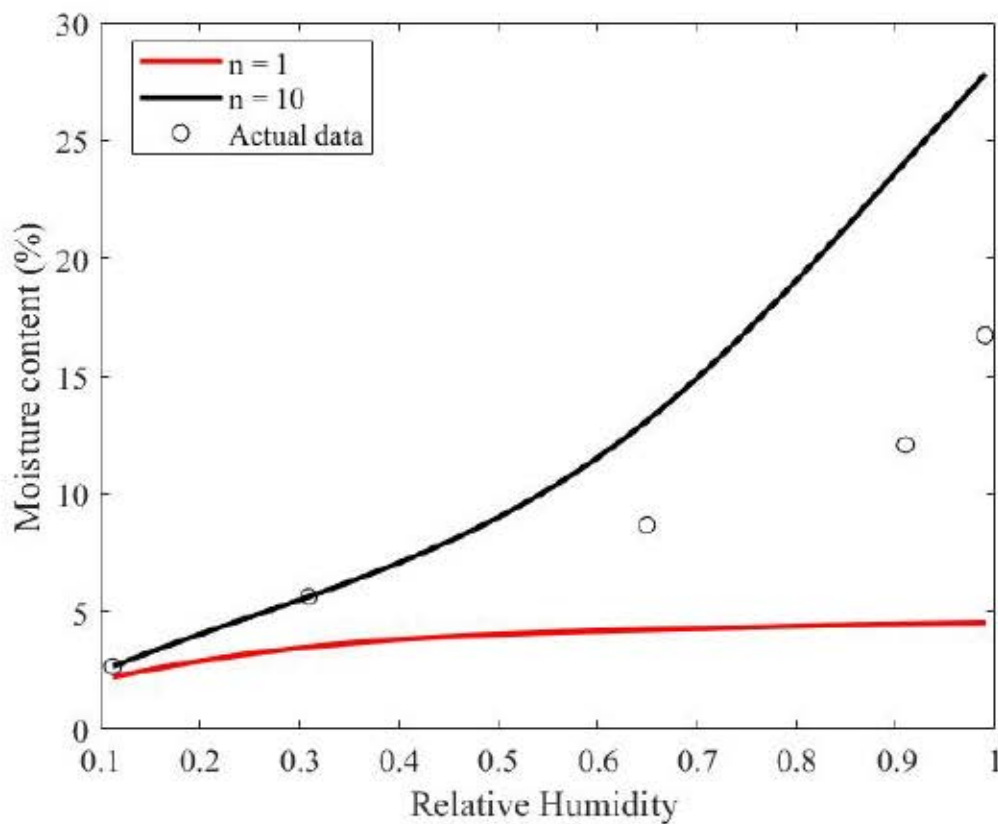


Figure 3.5: Fit of BET equation to water vapor sorption data for MCC. The value of $n = 1$ represents the monomolecular layer. It is also been plotted for the $n = 10$ number of layers.

comes out to be $182.5 \text{ m}^2/\text{g}$ [30], which is consistent with the literature as the model calculations of monolayers of adsorbed water show values around $120\text{--}190 \text{ m}^2/\text{g}$ [56].

As it is clear by looking at the numbers, the difference between the surface area for water and nitrogen is very large. This large difference between the surface area of water and nitrogen on the MCC surface indicates that the mechanisms of adsorption processes of water and nitrogen on the MCC is different from each other as found by Kocherbitov et al. [30], Ardizzone et al. [45] and Nam-Tran et al. [56].

Thermogravimetric analysis (TGA) is an analytical technique used in various

scientific and industrial applications to study the thermal properties of materials. TGA measures a sample's weight change as a function of temperature. At the same time, it is subjected to a controlled temperature program in an inert or oxidative atmosphere. The principle behind TGA is based on the fact that most materials undergo physical or chemical changes as they are heated, leading to weight loss or gain. TGA helps in identifying these changes and quantifying them. The thermal stabilities [45] of MCC are illustrated in Figure 3.6.

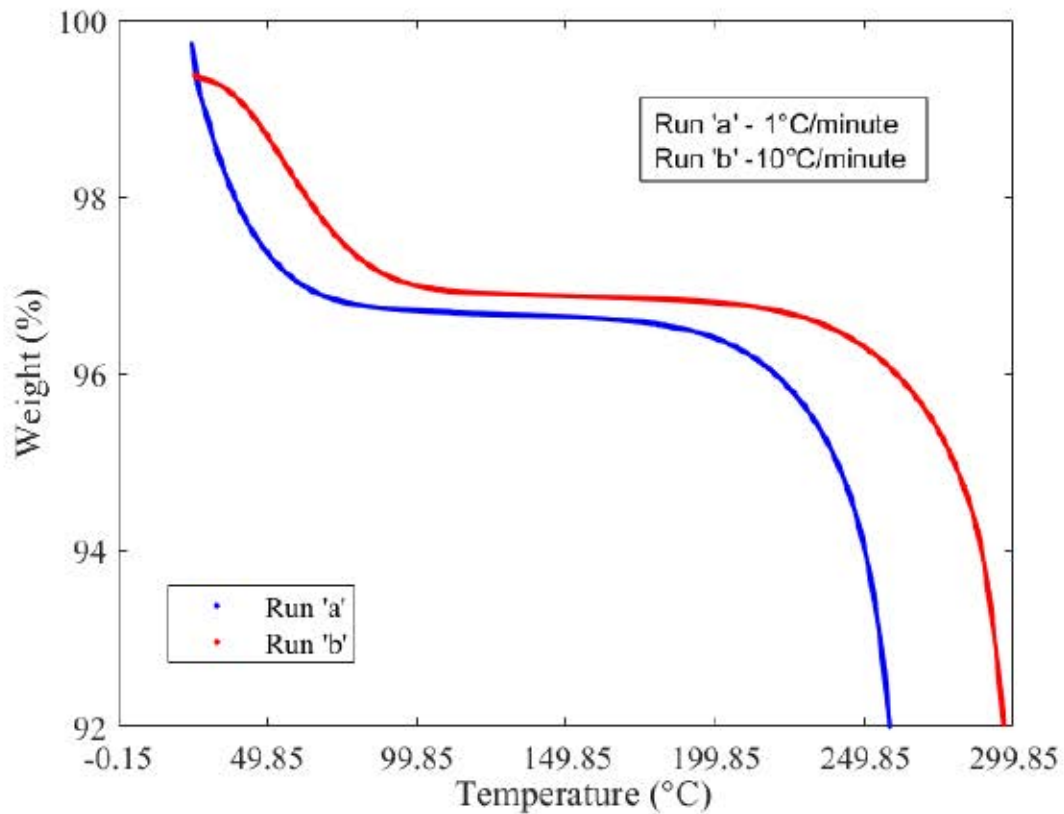


Figure 3.6: TGA analysis of MCC sample. Run (a) TGA performed at rate of 1° C Run (b) TGA performed at rate of 10° C.

The initial weight loss in Figure 3.6, in both of the runs, below 100° C, is attributed to the evaporation of the retained moisture from the MCC sample. After this initial, rapid, and small weight loss, the plateau region was noticed from tem-

peratures ranging from about 100° C to 200° C. The major weight loss was noticed after the plateau region in both runs in Figure 3.6, which is attributed to the final decomposition of the MCC sample. A similar trend was also found by Ardizzone et al. [45], where the variation in the scanning rates produced the variation in the weight loss and in the temperature range of the plateau region.

3.5 Summary

In this chapter, we used the BET theory to understand the water sorption and formation of water layers in MCC. According to this theory, the water first gets tightly bound at primary sorption sites at RH below 60%, and as the RH increases above 60% it starts to occupy secondary sorption sites. Therefore, from this understanding, a prediction can be made that at lower MC, the water gets sorbed on primary sorption sites and behaves like ice (irrotational water molecules). As the MC increases, the water is less tightly bound and therefore behaves like free water. Therefore, we should expect to see the transition between these two different states of water present in MCC as the moisture increases. BET sorption theory isotherms could also be used to measure the number of layers of water present in the composite system and study how the number of water layers changes as the moisture content is increased. The ultimate goal of using this theory was to find out the accurate thickness of the water layers present in the cellulose-water system but due to such a large variation in the surface areas found using Nitrogen and water, a large error in the prediction of accurate thickness was possible. Thus the accurate thickness was not measured in this thesis which helped us to modify our effective medium theory in Chapter 4 to a simple theory that did not involve any parameter directly related to the thickness of water. The TGA graphs also indicated the presence of differently bound water in MCC samples [57]. Below 100°

C, the sample mass rapidly declined due to the presence of loosely bound water molecules. At temperatures greater than 100° C, the sample is expected to contain tightly bound water and a major loss in sample weight was noticed at about 200° C where the sample is decomposed. Therefore, as the presence of differently bound water is indicated by the TGA analysis, we expect to see a change in the dielectric function of water in MCC with a change in MC (this will be further discussed in detail in Chapter 4). The study of this transition between ice and free water-like molecules in the MCC structure is the main focus of this thesis. This concept was further studied in Chapter 4 with the help of THz-TDS.

Chapter 4

Probing Water Dynamics in MCC using THz-TDS

4.1 Abstract

Terahertz time-domain spectroscopy was used to probe water dynamics in microcrystalline cellulose structures. To achieve this goal, the dielectric constant of water in microcrystalline cellulose (MCC) samples at different MCs was studied with the help of THz-TDS. With the application of THz-TDS, the amplitude and phase change were related to the absorption coefficient and refractive index of water absorbed into MCC samples. The absorption coefficient and index of refraction were then used to get the effective dielectric function of MCC at different MCs. Also, to investigate the dependence of the dielectric constant of water on the MC, a simple mixing theory model was used by taking two samples at different but similar MCs.

4.2 Introduction

Wood is made up of polymers like holocellulose and lignin, which are hydrophilic. The structure of these components contains hydroxyl and carboxylic groups. The hydroxyl groups are primarily responsible for wood-water interactions, but the carboxylic group can also interact with water. These chemical groups, which can attract water toward them in wood structures, are considered sorption sites.

Wood, being a hygroscopic material, experiences fluctuations in its MC based on the relative humidity (RH) and temperature (T). Its dimensional changes, whether swelling or shrinking, are directly tied to variations in MC. Under constant temperature and exposure to fixed RH, wood reaches an EMC of the same nature as its surrounding atmosphere. In this study, the MC is defined on an oven-dry basis as:

$$MC = \left(\frac{m - m_{od}}{m_{od}} \right) \times 100\% \quad (4.1)$$

As discussed in Chapter 3, water in wood can be found in two forms: bound and free. Bound water is chemically bound to the cell wall by intermolecular hydrogen bonds with the hydroxyl groups, and it behaves differently than free water. Therefore, from the perspective of the wood manufacturing industry, it becomes crucial to study the variation of MC in wood and its components. For the same reason, studying the dielectric function of water with changes in MC is essential.

THz-TDS has emerged as a significant tool in wood science due to its unique capabilities and transparency to frequencies below 1 THz. The dielectric relaxation response of water within the THz frequency range provides insights into the ability of water's permanent dipoles to respond to oscillating fields. When an electric field \vec{E} is applied, water molecules' permanent dipoles \vec{p} align with the field, inducing

polarization according to the following equation:

$$\vec{P} = \Sigma \vec{p} = (\epsilon - \epsilon_0) \vec{E}, \quad (4.2)$$

where ϵ_0 is the permittivity of the vacuum. Water molecules strive to reorient their dipole moments in line with the oscillating electric field. If the field frequency surpasses the water molecules' reorientation frequency, alignment becomes limited, reducing induced polarization and the dielectric constant. Therefore, the frequency-dependent dielectric response offers details about water molecule reorientation dynamics [19]. In the case of wood-water dynamics, water molecules have slower dynamics due to interaction with the cell wall; the water molecules become irrotational and are referred to as bound water.

In previous studies and experiments on wood, it has been found that the relaxation time of bound water molecules is different from the relaxation time of free water molecules and ice. It happens because the bound water molecules form strong hydrogen bonds with the available sorption sites in the wood cell wall as compared to the free water. Therefore, in wood, the dielectric constant of water varies depending upon the relaxation time of those water molecules [58] [59] (detailed discussion presented in section 4.4). As cellulose is the main composite of wood, one can expect to see a transition or change in the dielectric constant of water with the change in MC in MCC.

4.2.1 Effective Medium Theory

THz radiation is sensitive to water, so studying water dynamics in cellulose systems using THz is beneficial. As we already studied in the previous chapters, the properties of microcrystalline cellulose and wood vary significantly with changes in MC [60]. Effective medium models, often called effective medium theories

(EMT), are theoretical approaches to studying heterogeneous media. These models simplify the description of such complex materials by treating them as homogeneous media with effective properties. In this thesis, EMT is used to model the interaction of THz with the MCC. The following section discusses the overview and characteristics of the most commonly used EMT models. Below is an overview of the most commonly used EMT models and the parallel model which is used to study the dielectric function of water in MCC in this thesis.

4.2.1.1 Maxwell-Garnet Effective Medium Theory

The Maxwell-Garnet (MG) model is a well-known Effective Medium Theory (EMT) model used to investigate the effective polarizability of spherical inclusions inside a host matrix. This approach is applicable when the volume fraction of inclusions is low. The MG model is not generally used when there is a significant difference in permittivity between the inclusions and the host material. Its derivation is based on fundamental electrostatic principles and requires knowledge of the permittivity of the host material [19] [61] [62]. The effective permittivity ϵ_R of the composite system is defined as follows:

$$\frac{\epsilon_R - \epsilon_h}{\epsilon_R + 2\epsilon_h} = f_p \frac{\epsilon_p - \epsilon_h}{\epsilon_p + 2\epsilon_h} \quad (4.3)$$

In equation 4.3, the effective permittivity of the composite medium is represented by ϵ_R and ϵ_h represents the permittivity of the host material. The permittivity of the inclusions is given by ϵ_p and f_p denotes the volume fraction of inclusions.

In conclusion, the Maxwell-Garnet model is a valuable tool for assessing the electrical characteristics of composite materials, especially when dealing with low inclusion concentrations. When dealing with materials with a significant variation in permittivity between inclusions and the host, different models are frequently

used for understanding the electrical behavior of the composite.

4.2.1.2 Bruggeman model

In its most basic form, the Bruggeman model represents spherical particles embedded in a host material and can be employed when there is a considerable disparity in permittivity. The Bruggeman model's fundamental form is provided by [19] [63]:

$$1 - f_p = \frac{\epsilon_p - \epsilon_r}{\epsilon_p - \epsilon_h} \sqrt[3]{\frac{\epsilon_h}{\epsilon_R}} \quad (4.4)$$

The Bruggeman model can also be written in a more generic form, by combining the Polder and Van Santen approaches with it. This generic form is known as the extended Bruggeman (EB) model, and it can be written in its general form as follows [62]:

$$f_p = 1 - \frac{\epsilon_h^{[-\frac{3N^2+3N}{3N+1}]} (\frac{\epsilon_p - \epsilon_r}{\epsilon_p - \epsilon_h}) ((1+3N)\epsilon_p + (5-3N)\epsilon_h)^{[\frac{12N-18N^2-2}{9N^2-12N-5}]} }{\epsilon_R}, \quad (4.5)$$

where N is the depolarization factor that accounts for the geometry of the inclusions. These models are all used to represent the effective dielectric characteristics of mixtures in the THz region, but only under specified conditions. For example, the Maxwell-Garnett theory explained in the previous paragraph calculates the effective dielectric characteristics of a substance formed by dispersing small spherical particles inside a host material [61]. The Bruggeman model calculates the effective dielectric properties of many components in a mixture. Although there are many EMT models available, it is important to understand which EMT is most appropriate for the physical system being studied.

4.2.1.3 Parallel model: simple effective medium theory

Understanding the spatial organization or orientation of particles within a porous medium holds significant value in predicting its macroscopic properties. This knowledge and understanding can act as useful information for predicting the bulk properties of porous mediums. According to prior knowledge of the permittivity of composite mediums, one of the important assumptions for the EMT to work is negligible scattering. This condition can be satisfied by taking the electromagnetic wave, which has a wavelength much longer compared to the size of the particles in the composite medium.

Considering a specific porous medium, it is possible to envision a structured arrangement of its diverse constituents within a capacitor. As the capacitor can be connected in series and parallel, therefore, the pattern of arrangement of various constituents present in the porous medium can either be parallel, series, or a mixture or combination of both patterns [64]. In this thesis, the parallel connection of the phases in a composite medium is considered which is also represented in Figure 4.1. According to this theory, the inclusions are oriented parallel to the direction of the applied electric field, therefore, it will experience no screening effect. On the other side, if the inclusions are oriented in a completely perpendicular direction to an applied electric field it will create maximum screening over the composite medium, which gives the series model of EMT. This also indicates that the parallel or series model of EMT is equivalent to the form of capacitors connected in the parallel or series [64], respectively.

As in the parallel model [65] of EMT, all boundaries of inclusions are aligned in the direction parallel to the applied electric field, therefore giving no or negligible screening, providing the well-defined upper limit for the allowed range of ϵ of a composite. Therefore, the parallel model is the simplest model that we can use to understand the dielectric function of water in MCC providing the motivation of



Figure 4.1: Pictorial representation of a three-phase striped composite medium, where red arrow indicates the direction of the electric field.

using this theory in the present study.

The parallel model [64] [65] gives the effective property ψ_{eff} as a linear function of the properties of the continuous and dispersed phases, with a volume fraction of the dispersed phase given as ϕ . It can be represented as

$$\psi_{eff} = (1 - \phi)\psi_c + \phi\psi_d \quad (4.6)$$

To describe this theory, let us consider two materials, one with high MC and the other with low MC. Let's say that the material with high MC has a dielectric constant of ϵ_B , and the sample with low MC has a dielectric constant of ϵ_A . Therefore, according to the simple mixing rule, we can write,

$$M_h = M_l + M_w \quad (4.7)$$

where M_h is the mass of the sample with high MC, M_l is the mass of the sample with low MC, and M_w is the additional mass of the water. Similarly, we can write the density for the sample with high MC and low MC in terms of the volume fraction of low MC (f_l) and volume fraction of water (f_w) according to the following

relation:

$$\rho_h = f_l \rho_l + f_w \rho_w, \quad (4.8)$$

such that

$$f_l + f_w = 1. \quad (4.9)$$

By using these equations, we can find the value of f_w . From equation 4.9 we have:

$$f_l = 1 - f_w \quad (4.10)$$

By using equation 4.10 in equation 4.8 we get:

$$\rho_h = (1 - f_w) \rho_l + f_w \rho_w \quad (4.11)$$

After simplifying the equation, we have:

$$\rho_h = \rho_l + f_w (\rho_w - \rho_l) \quad (4.12)$$

Therefore, f_w becomes:

$$f_w = \frac{\rho_h - \rho_l}{\rho_w - \rho_l} \quad (4.13)$$

In terms of mass and volume of high and low MC, and also by considering $V_h = V_l = V$, the final equation becomes:

$$f_w = \frac{M_h - M_l}{V \rho_w - M_l'} \quad (4.14)$$

therefore, for this effective medium theory, the volume fraction of water can be found by using relation 4.14. Once the value of f_w is known, the value of f_l can be calculated by using equation 4.10.

After the volume fractions are calculated, the simple EMT can be used to calculate the dielectric constant of water from measured THz data.

In Chapter 2, we discussed the details of how dielectric properties can be extracted using THz measurements. The following paragraph will discuss how we can incorporate the experimental measurements into the EMT. Therefore, from Chapter 2, we know that if $E_A(\nu)$ is the electric field amplitude of the reference measurement $E_B(\nu)$ is the electric field amplitude of the transmitted field, both can be related as follows:

$$\frac{E_B(\nu)}{E_A(\nu)} = t_{AB}t_{BA} \exp(i\frac{2\pi\nu L}{c}(\hat{n}_B - \hat{n}_A)) \quad (4.15)$$

The product of t_{AB} and t_{BA} is almost equal to 1. Therefore, equation 4.15 can be written in a simplified manner as:

$$\frac{E_B(\nu)}{E_A(\nu)} \simeq \exp(i\frac{2\pi\nu L}{c}(\hat{n}_B - \hat{n}_A)) \quad (4.16)$$

Here, \hat{n}_B and \hat{n}_A are the complex index of refraction for samples B and A, respectively.

Now, according to equation 4.6, the effective index of refraction can be written as:

$$n_{eff} = f_A \hat{n}_A + f_B \hat{n}_B \quad (4.17)$$

Also, we can write:

$$\hat{n}_B = f_A \hat{n}_A + f_w \hat{n}_w, \quad (4.18)$$

where \hat{n}_w is the complex index of refraction of water. After utilizing equation 4.18 in equation 4.16, the equation becomes:

$$\frac{E_B(\nu)}{E_A(\nu)} = \exp\left(i\frac{2\pi\nu L}{c}(f_A \hat{n}_A + f_w \hat{n}_w - \hat{n}_A)\right), \quad (4.19)$$

which reduces to:

$$\frac{E_B(\nu)}{E_A(\nu)} = \exp\left(i\frac{2\pi\nu L}{c}(f_w(\hat{n}_w - \hat{n}_A))\right) = \exp\left(i\frac{2\pi\nu L}{c}\right) f_w \hat{N}, \quad (4.20)$$

with:

$$\hat{N} = \hat{n}_w - \hat{n}_A. \quad (4.21)$$

Using equation 4.20, the value of the complex index of refraction, $\hat{n}_w = n_w + ik_w$, can also be obtained, where the real part represents the index of refraction (refer to equation 2.7) and the imaginary part is used to obtain the absorption coefficient (refer to equation 2.8). Because this equation depends on the thickness of the sample (L) directly, therefore instead of using equation 4.20, a very simple approach was taken and equation 4.18 was directly used to get the dielectric function of water. Also, in the preliminary analysis, the results using equation 4.20 were found to be noisy, therefore, this method alongside other effective medium theory models could be further studied in the future to improve the results.

Thus, the simple effective medium theory (equation 4.18) was used to study the real and imaginary parts of the dielectric function of water in MCC by using the measurements of the real and imaginary parts of the dielectric function of MCC. This will be elaborated on in detail in the upcoming sections.

4.3 Materials and Methods

The following sections summarize the preparation of MCC samples for the THz sample measurements. Also, the key details about the system and technology used for the data collection are discussed.

4.3.1 Sample preparation

The samples of MCC were obtained from Sigma-Aldrich. The samples were oven-dried in a convection oven for 24 hours at $100\pm 2^{\circ}\text{C}$ to determine the oven-dried mass of the MCC. Once the powder was oven-dried, approximately 15 (± 0.02) grams of MCC was weighed on a ULINE balance scale (Model H-9884) with an accuracy of 0.01 grams and transferred to a transparent petri dish with 100 mm \times 15 mm dimensions. The powder was then settled with the help of 0.75g vibrations created by using an air compressor on the optical table for at least five minutes. The vibration data was recorded with the help of a Physics Toolbar application downloaded on a mobile phone. Once the thickness of the powder was uniform, the pre-measurements of thickness and mass were taken. Afterward, the filled Petri dishes were conditioned at different relative humidities (RH) to obtain different MC's. The MCC is conditioned with the help of desiccators, having constant RH with the help of saturated salt solutions. The saturated salt solutions contained Lithium Chloride (LiCl, RH = 11.3%), Calcium Chloride (CaCl_2 , RH=31%), Potassium Fluoride (KF, RH=65%), Sodium Sulphate (Na_2SO_4 , RH=91%), water (H_2O , RH=99%) obtained from SIGMA-ALDRICH. The saturated salt solution and their corresponding RH% are summarized in Table 4.1.

Saturated Salt Solution	Relative Humidity (RH%)
Lithium Chloride	11.3
Calcium Chloride	31
Potassium Fluoride	65
Sodium Sulphate	91
Water	99

Table 4.1: Saturated salt solutions and their corresponding RH% used for conditioning the MCC samples.

The samples were left in the desiccators for at least 48 hours to make sure that they had reached EMC. Once equilibrium was reached, the samples were re-

moved from the desiccators and vacuum-sealed using a commercial vacuum sealing unit. The vacuum-sealed MCC samples were weighed before and after each THz measurement to ensure that MC did not change during the measurements. Three samples for each MC were prepared, and THz measurements were repeated three times for each sample of every MC at four different orientations of the sealed samples: 0° , 90° , 180° , and 270° and averaged. This stepwise process of sample preparation to THz spectral measurements is summarized in Figure 4.2. The conditioning of the MCC samples and THz experiments was conducted at room temperature ($21 \pm 1^\circ\text{C}$). The physical dimensions and the mass of the MCC samples were used to get the density and MC of the samples.

4.3.2 THz spectral measurements

In this thesis, the THz spectroscopy of MCC was performed using a transmission geometry. The transmission measurements of the MCC samples were performed using a Picometrix T-Ray 5000 THz spectrometer. The T-Ray 5000 spectrometer generates THz signals at a rate of 100 waveforms per second in an 320 ps window having bandwidth from approximately 0.1-2 THz, with a THz beam diameter (1/e electric field) of approximately 30 mm. The basic setup is indicated in Figure 4.3.

The petri dishes were marked with 4 different orientations: 0° , 90° , 180° and 270° . The measurements were recorded at all four orientations for all the samples to average out non-uniformity in thickness. Non-uniformity in thickness can lead to variations in the measured density of the material. This can affect the interaction of light with the material, leading to different indices of refraction and absorption coefficients at different points in the sample area. It can also be seen from equations 2.7 and 2.8 (Chapter 2) that the index of refraction and absorption coefficients are inversely proportional to the thickness; therefore, it is important to take measurements at all four orientations to average out the non-uniformity due to varying

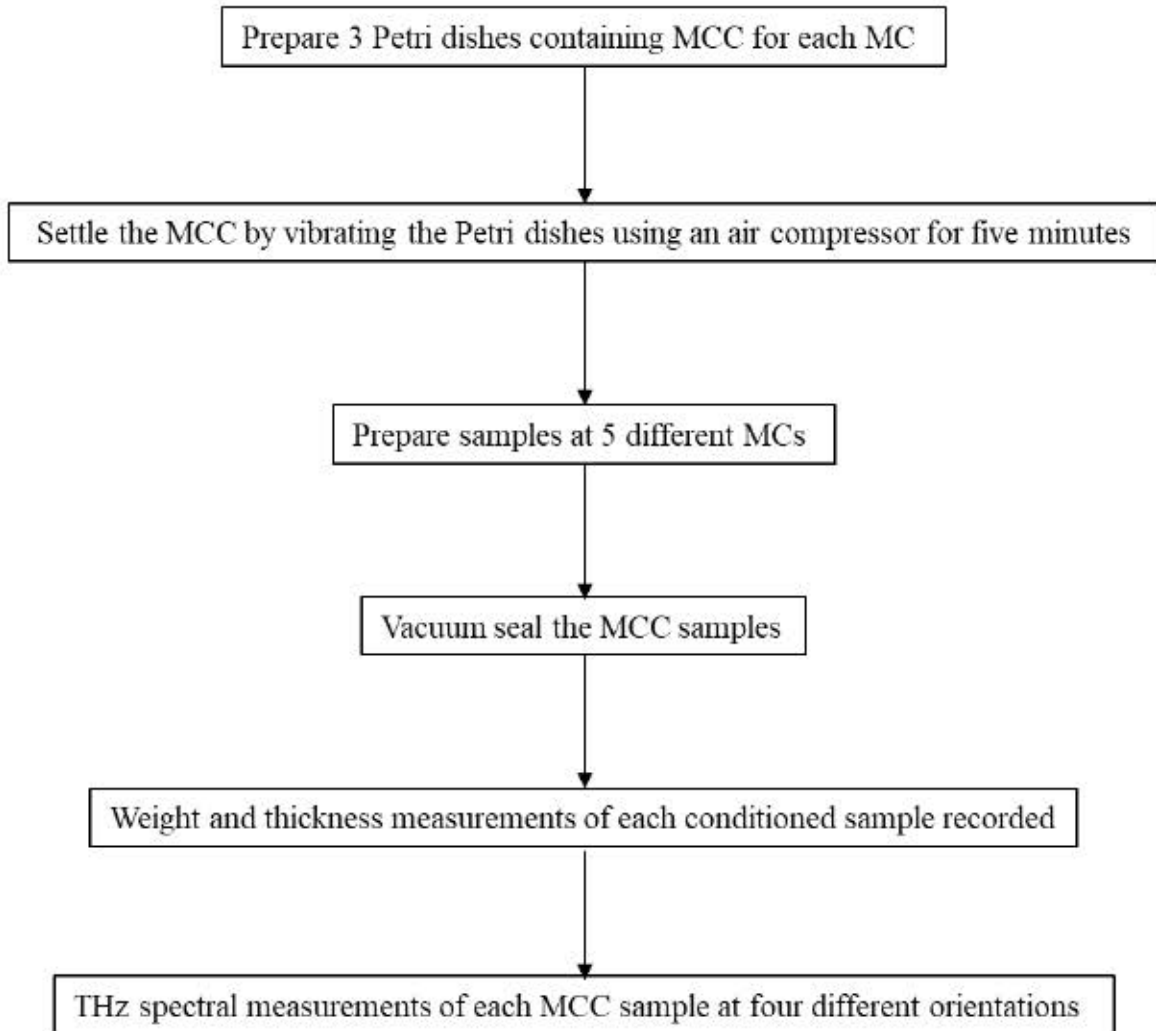


Figure 4.2: Flowchart showing the step-wise process of sample preparation to THz spectral measurements.

thickness. Before each transmission measurement, a reference measurement was taken with an empty, vacuum-sealed petri dish in the path of the THz beam (both the reference empty and sample petri dishes were vacuum-sealed so that the difference between the reference and transmitted THz gave only information about the MCC). After taking the THz measurements, the complex index of refraction for MCC at different MCs was measured. The measured complex index of refraction was then used to get the complex dielectric function of MCC at different MCs, which was then combined with effective medium theory to get the complex dielec-

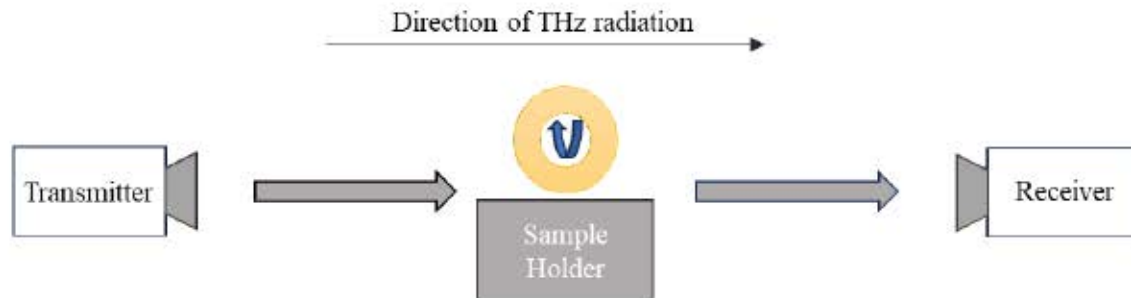


Figure 4.3: The representation of basic setup used to make THz spectral measurements of MCC samples.

tric function of water in MCC. The flowchart indicating the measurement process for the acquisition of the dielectric function of water is shown in Figure 4.4.

4.4 Results and Discussion

Water in microcrystalline cellulose causes a reduction in transmitted THz pulse amplitude and a temporal shift of the THz pulse in the time domain. These two values relate to the frequency-dependent complex refractive index of microcrystalline cellulose. Figure 4.5 depicts a typical THz pulse passing through a microcrystalline cellulose sample, with MC ranging from 2.65% to 16.73%.

The THz field diminishes with increasing MC, as shown in Figure 4.5. As expected from previous studies, in Figure 4.5, the lowest MC, specifically at 2.65%, exhibits the highest amplitude and manifests an earlier arrival time in comparison to both the amplitude and phase shift observed at higher MCs. The reason behind this phenomenon is the pronounced absorption of THz radiation by water molecules. As discussed in Chapter 1, it is essential to recognize that THz radiation interacts strongly with water molecules due to their dipole nature. Therefore, variation of the MC within a material also alters its optical response to THz radiation. As MC rises, the attenuation of THz radiation intensifies, leading to a reduction in pulse amplitude and a consequential delay in the arrival time of the pulse.

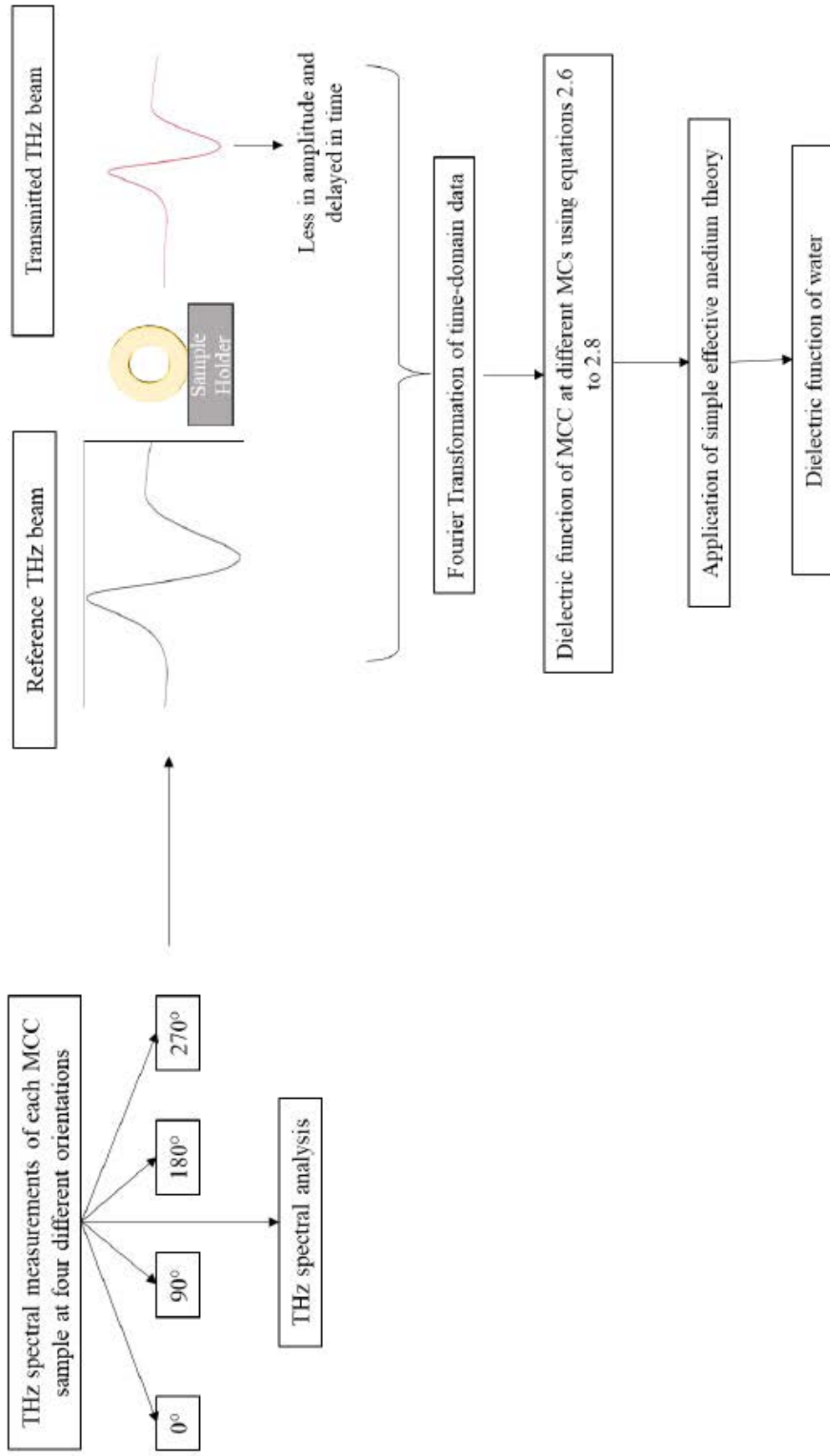


Figure 4.4: The flowchart shows the measurement process of obtaining the dielectric constant of water using the THz spectral measurements.

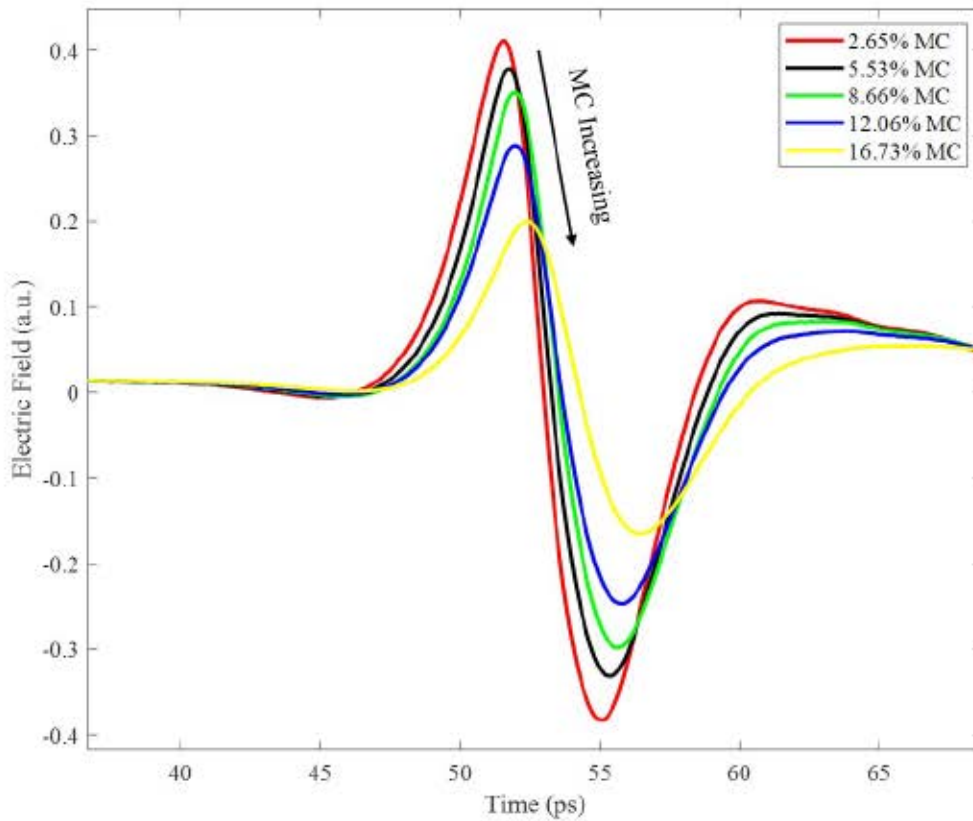


Figure 4.5: Variation of THz field amplitude in time for variable MC in MCC samples. As the MC gets higher in MCC samples, the THz field amplitude decreases, and the THz pulse comes later in time (phase shift or time delay).

The data in the time domain was Fourier transformed to the frequency domain. The relationship between the dielectric function ($\epsilon(\nu) = \hat{n}^2(\nu)$) and the complex index of refraction is used to get the frequency-resolved real and imaginary parts of the dielectric function, (ϵ). Figure 4.6 represents the measured frequency-resolved real part of the dielectric function obtained from the THz spectroscopy of the MCC at various MCs. The imaginary part of the frequency-resolved dielectric function is shown in Figure 4.7. It can be noted in both Figures 4.6 and 4.7 that the real and imaginary parts of the effective dielectric function of the MCC is changing monotonically with a change in MC. As per literature [66] [19], the water below 10% MC in wood is mostly bound, and at high MC (usually above 30% MC), the

water is mostly free. Therefore, as the nature of the water varies with the increase in MC, we are expecting that the dielectric function of water in MCC will also change with MC. A similar study has already been reported on wood [66], where they defined four ranges of MCs to estimate the influence of water on the dielectric properties of wood. The four ranges of MC and the type of moisture associated with them are given in Table 4.2.

Type of Moisture	Moisture Content Range (%)
Monomolecular moisture	Oven-dry wood to 5% MC
Polymolecular moisture	5% to 18-23%MC
Capillary condensed moisture	18-23%MC to upto fiber saturation point MC
Free water	Above fiber saturation point (30% MC)

Table 4.2: The four ranges of MC and the associated type of moisture with them. As adapted from Torgovnikov G.I. 1993

According to this reported study on wood [66], the water associated with a monomolecular layer interacts most strongly with the cell wall of wood. With an increase in water content, the number of layers of water molecules increases, and therefore, the interaction between the cell wall and adsorbed water starts to diminish [66]. Above 23% MC and up to the fiber saturation point, the moisture starts approaching the capillary condensed form of MC, and the properties of this type of water are found in between the properties of adsorption and free water. Therefore, three types of bound water can be distinguished in wood, i.e., monomolecular, polymolecular, and capillary condensed water [66]. Monomolecular water has the most bond energy, and capillary condensed water has the least. As cellulose is the primary component of wood, therefore, in this thesis, we tried to perform the same study on MCC by taking only the first two kinds of bound water, i.e., monomolecular moisture and polymolecular moisture, and free water into consideration. As

the transition between these borders of bound water and free water is unknown, this thesis revolves around the aim of finding the changes in the nature of water as the transition process occurs.

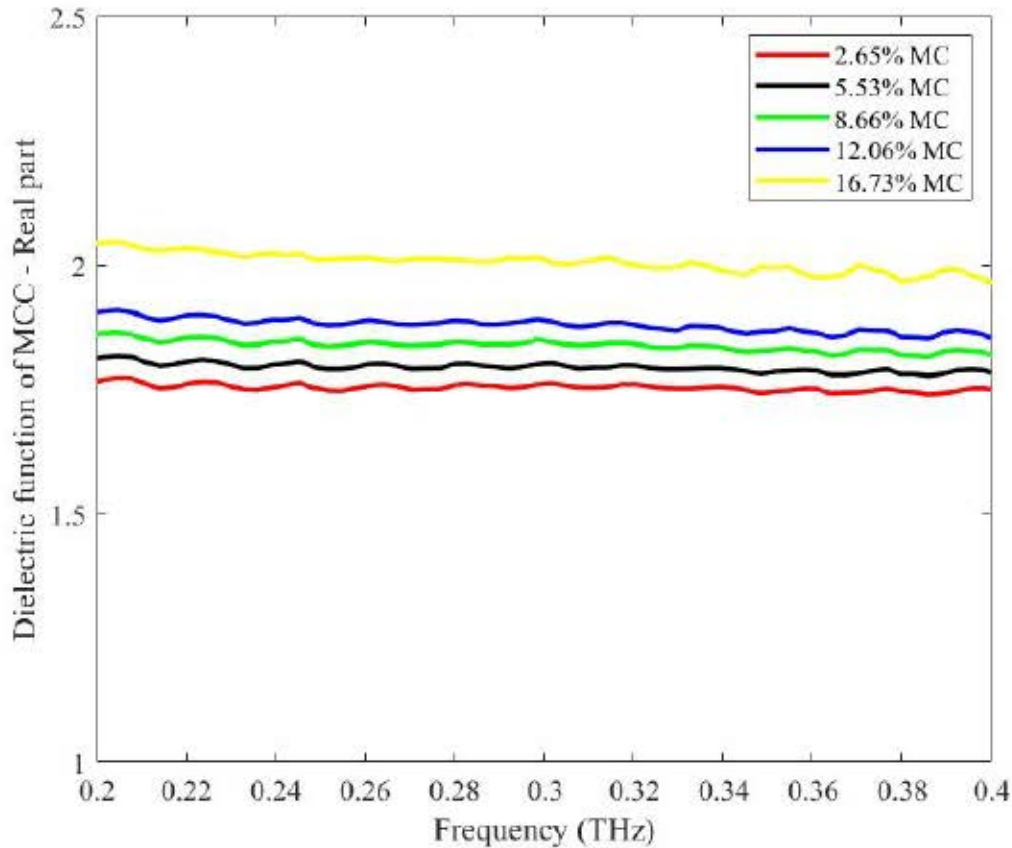


Figure 4.6: Variation of the real part of the dielectric function of MCC with respect to frequency obtained using THz transmission spectroscopy. This figure shows the real part of the dielectric function of MCC increases with an increase in MC.

Figures 4.8 and 4.9 show the real and imaginary parts of the dielectric function of MCC as a function of MC determined at a frequency of 0.2 THz. These graphs were plotted to see the variation of the dielectric constant of MCC at a constant frequency of 0.2 THz as the MC in MCC changes. The frequency of 0.2 THz is chosen because the signal-to-noise ratio reaches its maximum at this frequency. As indicated in these Figures (refer to Figures 4.8 and 4.9), both the real and imaginary

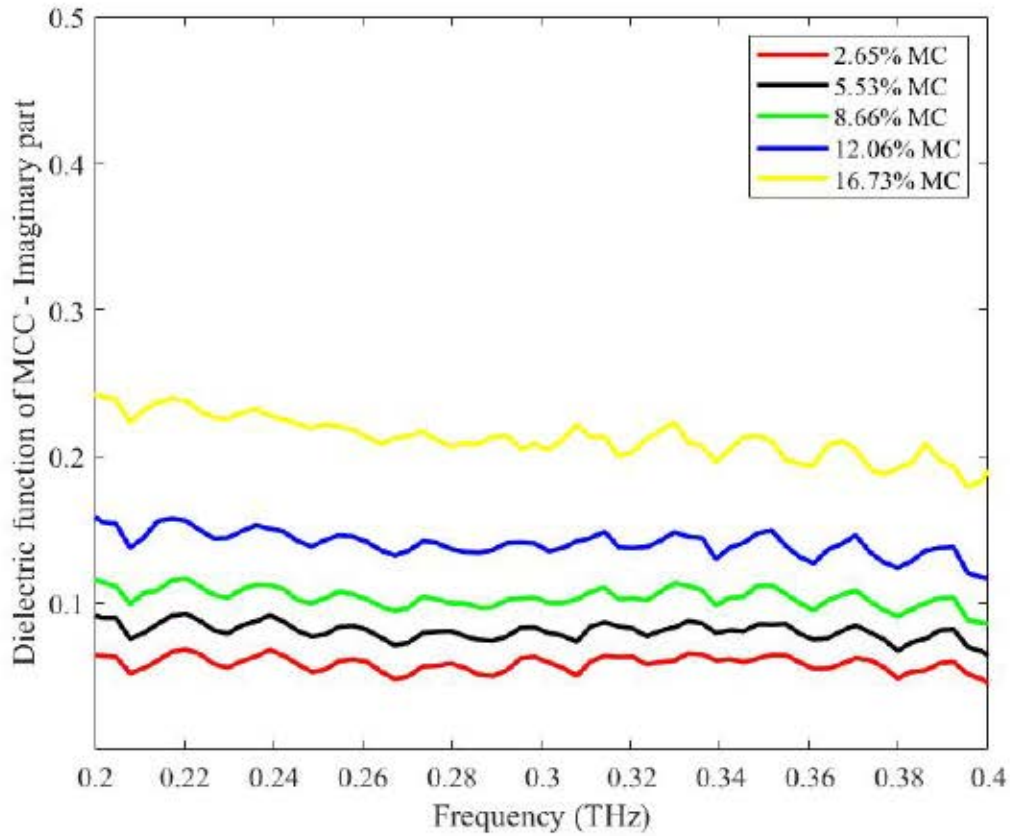


Figure 4.7: Variation of the imaginary part of the dielectric function of MCC with respect to frequency obtained using THz transmission spectroscopy. This figure shows the imaginary part of the dielectric function of MCC increasing with increasing MC.

parts are dependent on the MC in the MCC. The results shown in Figure 4.8 and Figure 4.9 clearly predict that the real and imaginary parts of the dielectric function of MCC increase with increasing MC, as expected. This also gives us an idea that the dielectric function of water in MCC should vary with varying MC. To get the result, these measurements could now be combined with EMT.

To determine the dielectric constant of water from these THz measurements, we can now develop a model that describes the relationship of the dielectric constant with other factors. Different models are available, for example: Bruggman effective medium theory, the Maxwell-Garnet effective Medium theory, and the

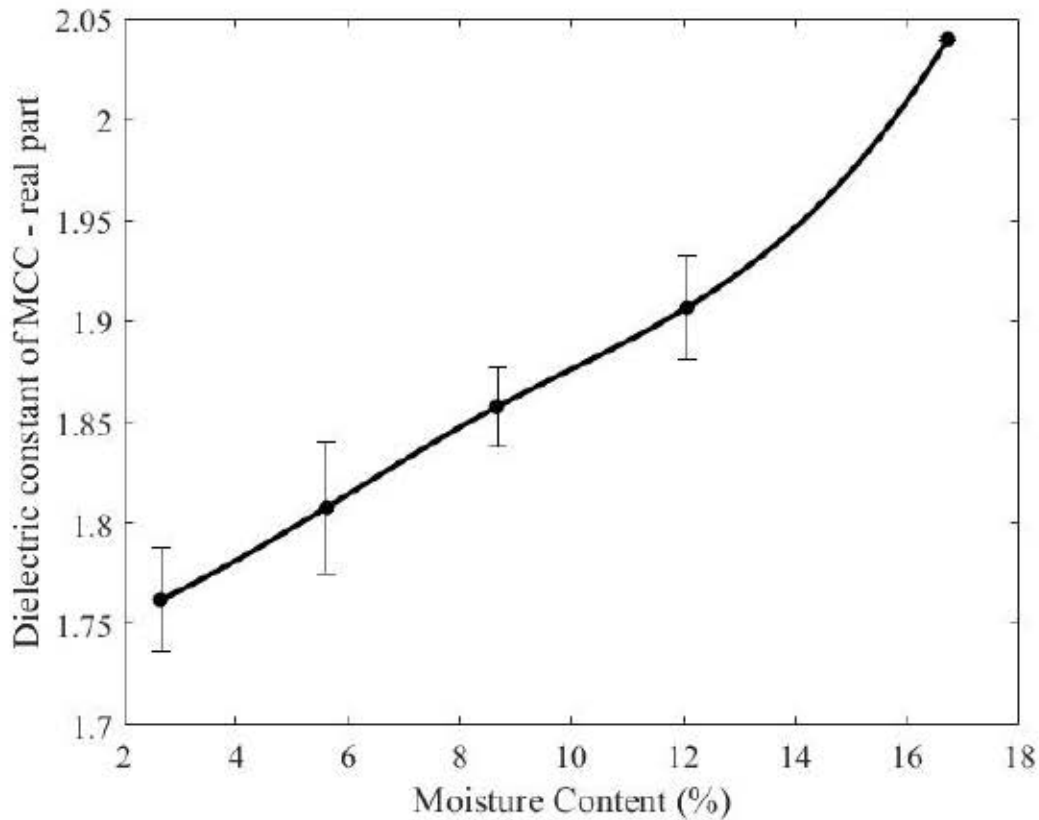


Figure 4.8: Variation of the real part of the dielectric function of MCC with respect to MC(%) obtained using THz transmission spectroscopy at a frequency of 0.2 THz.

parallel model, as discussed in section 4.2.1. The simple effective medium theory is the easiest way to get information about the dielectric response of water in MCC structures as compared to other EMTs. Therefore, in this thesis, the simple mixing effective medium theory was used to extract the dielectric constant of the water from the THz measurements at different MCs which are suitable for studying the trend. Once the prediction about the transition of the dielectric function of water in MCC is made, the EMT model can be modified to acquire more precise results. To get the dielectric constant of water at a certain MC, two different THz measurements from the samples whose MC is close are needed. As we already know, the dielectric function of water varies with increasing MC; therefore, taking two MCs that are far apart from each other will only provide the average dielectric constant

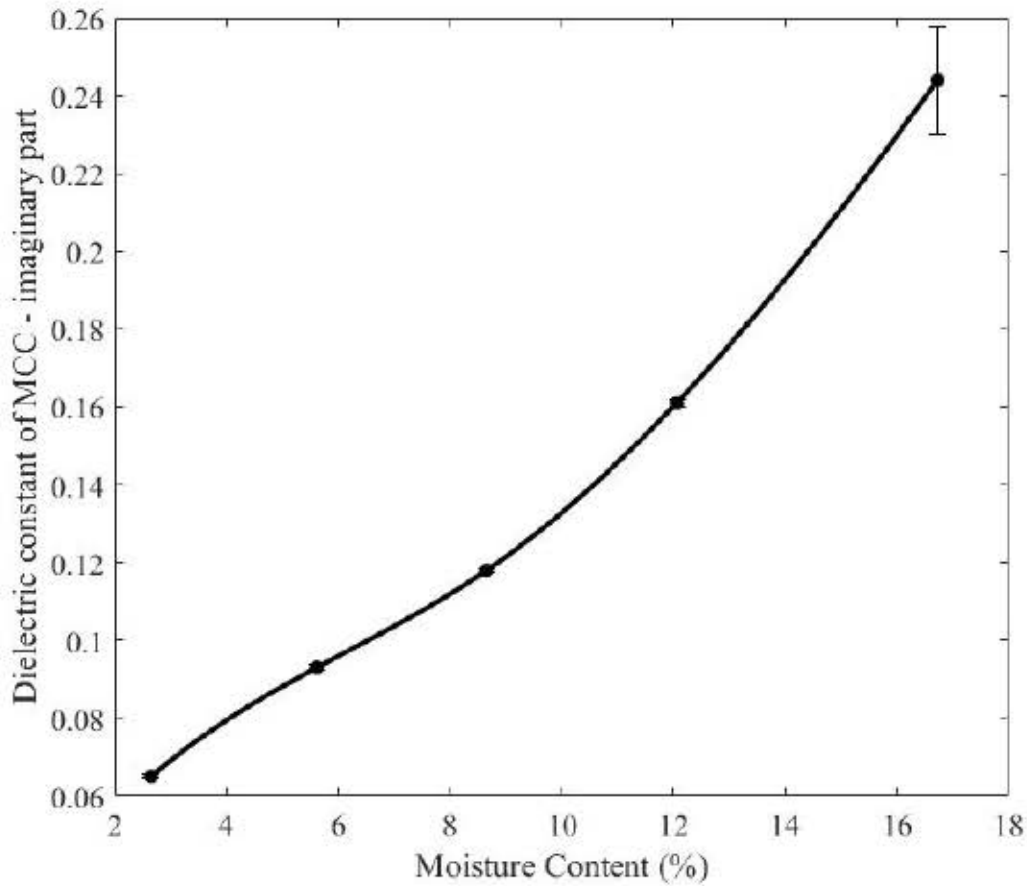


Figure 4.9: Variation of the imaginary part of the dielectric function of MCC with respect to MC(%) obtained using THz transmission spectroscopy at a frequency of 0.2 THz.

of water over that range of MCs.

4.4.0.1 Prediction of the dielectric function of bound water from THz measurements

From the results of the dielectric function of MCC (as represented in Figures 4.6 and 4.7), it can be seen that with changes in MC, the effective dielectric function of MCC also varies. To predict the dielectric function of water, consider the very simple view that the system has the simplest two-phase laminar configuration with alternating layers of two materials having a complex index of refraction \hat{n}_A and

\hat{n}_B [67]. For the electric field applied parallel to the laminations, the simple effective medium approximation can be described by equation 4.22 [67]. Therefore, in this thesis, a simple mixing theory model can be applied to predict the effective dielectric function of water in MCC. The effective medium approximation for the simple mixing rule for two samples of MCC having comparable MCs can be described by (see subsection 4.2.1.3):

$$\hat{n}_{eff} = f_A \hat{n}_A + f_B \hat{n}_B \quad (4.22)$$

where \hat{n}_A is the complex index of refraction of the first material, \hat{n}_B is the complex index of refraction of the second material, and \hat{n}_{eff} is the complex index of refraction of the mixture. In equation 4.22, f_A and f_B represent the corresponding volume fractions for the first material and second material, respectively. As it is clear from equation 4.22, to get the complex index of refraction for the water in MCC at a certain MC, we need to measure the complex index of refraction of MCC at two different MCs. In this thesis, we have taken the two MCs that are close to each other because: (1) To get a dielectric function of water at some specific MC, it makes sense to take and compare the two MCs that are close to that specific MC value. (2) If we compare two MCs that are far apart from each other to study the dielectric function of water in MCC, the result will only give us the average dielectric constant of water over that range, which will give no new information (as we already know that the dielectric constant of water varies with varying MC).

In this thesis, \hat{n}_A is taken as the complex index of refraction for the lower MC sample, and \hat{n}_{eff} is considered the complex index of refraction for slightly higher MC. In this way, we can obtain the value of \hat{n}_B using the THz spectral measurements, which will give us the complex index of refraction of water (refer to the procedure indicated in Figure 4.4). The appropriate volume fractions can be obtained by using equations 4.14 and 4.10. To compare the obtained dielectric constant of

water at a particular MC, the dielectric constants of ice and water were used in Figures 4.10 and 4.11 as lower and upper bounds, respectively.

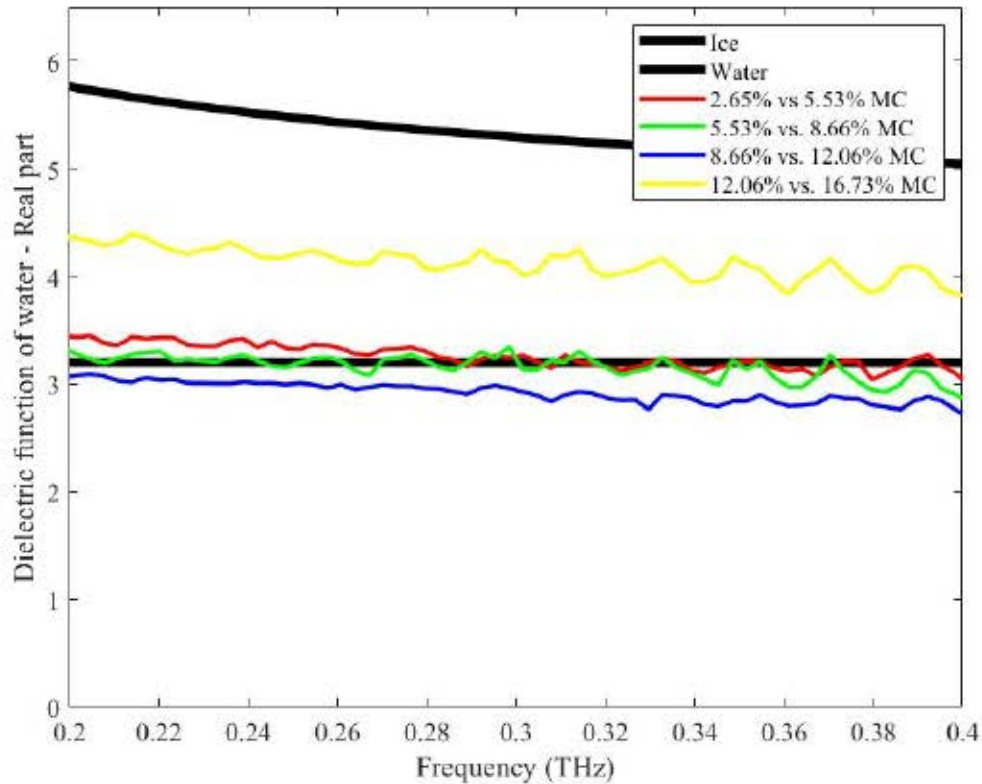


Figure 4.10: Variation of the real part of the dielectric function of water with respect to frequency obtained using THz transmission spectroscopy.

As seen in Figures 4.10 and 4.11, both the real and imaginary part of the dielectric function of water vary with MC. The following process defines the adsorption of water molecules onto the sorption surface.

The initial water molecules added to the oven-dried MCC at the lowest MC had most of the sorption sites available, resulting in a very tight bonding of the water molecules to the sorption surface. These tightly bound water molecules behave as irrotational water molecules, which have a larger relaxation time and, consequently, a lower dielectric constant, per the Debye model [58] [59]. As the MC is

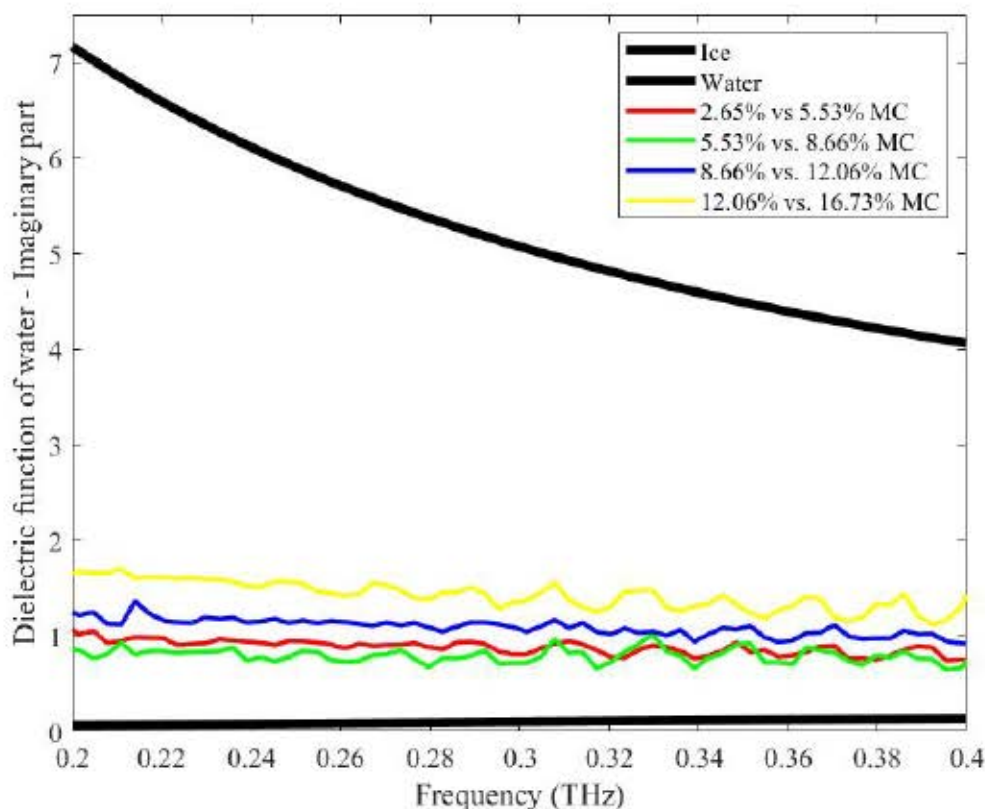


Figure 4.11: Variation of the imaginary part of the dielectric function of water with respect to frequency obtained using THz transmission spectroscopy.

increased in the MCC samples, the primary sorption sites get filled, and the new incoming water molecules get occupied in the secondary layers; thus, the molecules move away from the sorption surface. As this happens, the water molecules now present in the secondary layers are more free to rotate and thus have a shorter relaxation time [59] [68]. This shorter relaxation time results in a larger dielectric constant for those water molecules. Therefore, when MC increases, the dielectric constant of water in MCC increases. Therefore, as explained in reference [59], there are two important factors to look upon to understand the change in dielectric response of water with respect to change in MC: (1) With a decrease in hydration level or MC, the relative number of irrotational water molecules becomes more prominent. (2) With an increase in the MC, the irrotational water molecules start

getting converted into water molecules that are freer to rotate or those that exhibit bulk-like behavior. This dynamic behavior of water can be easily understood by having a look at a double Debye model, as explained in the next paragraph.

The dielectric response of water has been analyzed with the help of the double Debye model with two relaxation times, as thoroughly described in reference [19] [58] [69]. This double Debye approach is based upon the molecular interaction between water molecules present in MCC and the THz radiation. The double Debye model for the frequency-dependent dielectric function of water can be described as [58] [59] [68] [70]:

$$\epsilon(\omega) = \frac{\epsilon_s - \epsilon_1}{1 - i\omega\tau_1} + \frac{\epsilon_1 - \epsilon_\infty}{1 - i\omega\tau_2} + \epsilon_\infty \quad (4.23)$$

where ϵ_s is the static permittivity at low frequency, ϵ_∞ is the limiting permittivity at high frequency, and ϵ_1 is the transitional dielectric constant between two relaxation processes. τ_1 and τ_2 represent the two relaxation time constants for slow and fast relaxation processes, respectively. The slow and fast relaxation processes of water may involve translational and rotational diffusion, hydrogen bond rearrangement, and structural rearrangement, depending on the time scale [70]. Therefore, the double Debye model presents two relaxation processes, and these two processes represent the impact of externally applied THz radiation on the water molecules. For example: when THz radiation excites the water molecules, the natural tetrahedral structure of water (also referred to as water "cage" in reference [70]) tries to reorient. To reorient, there must be a breakage of four hydrogen bonds (the cage must break). This process is known as the "slow relaxation process." Therefore, after some relaxation time τ_1 , the single water molecule will reorient and move to a new tetrahedral site in time τ_2 , which is a fast process. Therefore, the water molecules that are associated with relaxation time τ_2 are also referred to as "fast" water molecules [59]. Moreover, using the double Debye model (refer to

equation 4.23), we can interpret that at the limit, the two relaxation constants, i.e., τ_1 , and τ_2 go to infinity, so we get irrotational water. At this limit, the dielectric function of water molecules becomes equal to ϵ_∞ , which is a real number that has a value of 3.49 (reported by reference [58]). When compared to the value of the dielectric function of ice that has been plotted in our results (refer Figure 4.12), the value of the real part of the dielectric constant of water using the double Debye model at the limit when τ_1 and τ_2 go to infinity came out to be very close.

For low MC, the dielectric constant was expected to be very close to the dielectric constant of bound water (similar to ice), as the water molecules are irrotational. For higher MC, the dielectric constant of water should approach the dielectric constant of free water as the rotational degree of freedom is available again. As expected, our findings also indicate the presence of both irrotational and free water molecules in the MCC, which are discussed next.

The red, green, and blue curves in Figures 4.10 and 4.11 indicate that the dielectric constant of water at very low MC is close to that of ice, and this has happened to the water molecules that got adsorbed under 12% MC. As more water molecules started entering the sample at higher MC, more hydrogen bonds were broken, which eventually created more available sorption sites. This increases the relaxation time and increases the dielectric constant for the highest MC (indicated by the yellow curve in Figures 4.10 and 4.11). In this thesis, only the MCs up to 16.73% were prepared, but even the higher MCs can be prepared, and eventually, at a certain higher MC, it is expected that the dielectric properties of bound water will become similar to the dielectric properties of free water in MCC. This also implies that, at a certain MC, a further change in MC will not impact or change the dielectric properties of water. No change in the dielectric properties of water will also indicate that all the sorption sites are not attached to bound water, and new additions of water molecules will be stored as free water.

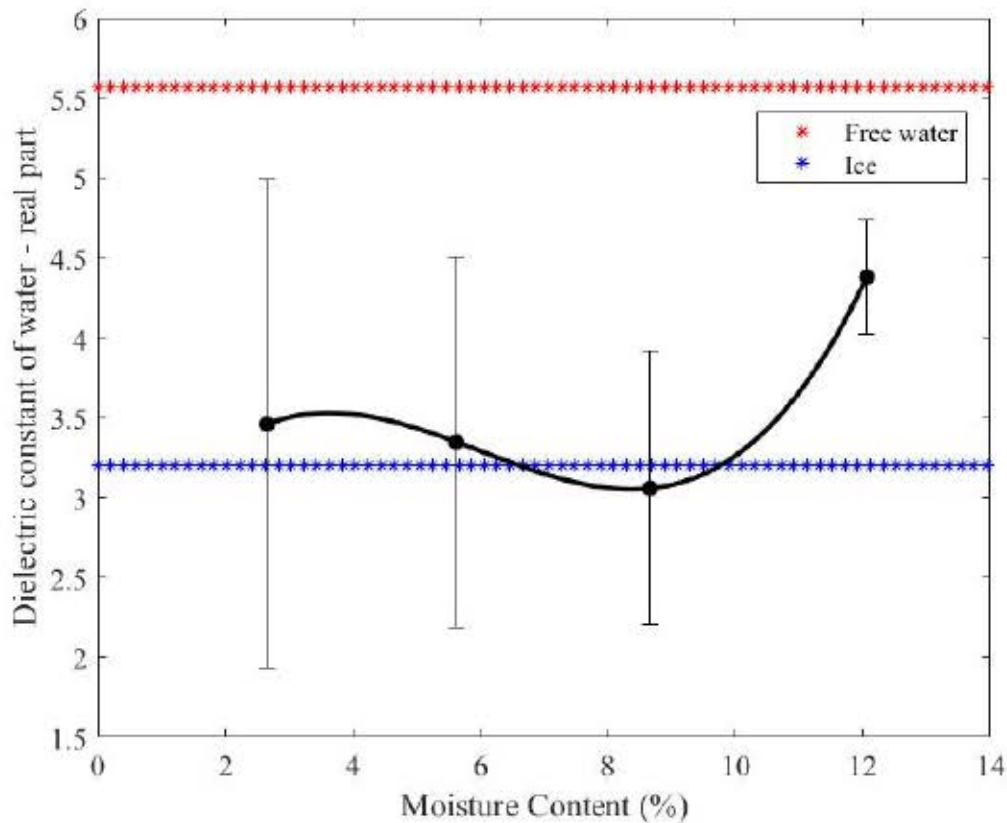


Figure 4.12: Variation of the real part of the dielectric function of water with respect to MC obtained using THz transmission spectroscopy at 0.2 THz.

Figures 4.12 and 4.13 discuss the dependence of the real and imaginary parts of the dielectric function of water on MC with the help of a smooth curve at 0.2 THz. As one can notice in Figure 4.12, the error bars for the comparison of red, blue, and green curves in Figure 4.10 are relatively large as compared to the error found for the yellow curve in Figure 4.12. As the actual trend or a function that clearly defines the relationship between the dielectric function of water in MCC is unknown, we have used a smooth curve, and this smooth curve has been chosen as we expect that the real part of the dielectric function of water (refer to Figure 4.12) will be constant or the water molecules will behave as irrotational until around 10% MC and will then increase after 12% MC. This could be tested by taking MC at or above the fiber saturation point, which is discussed in the future work section in

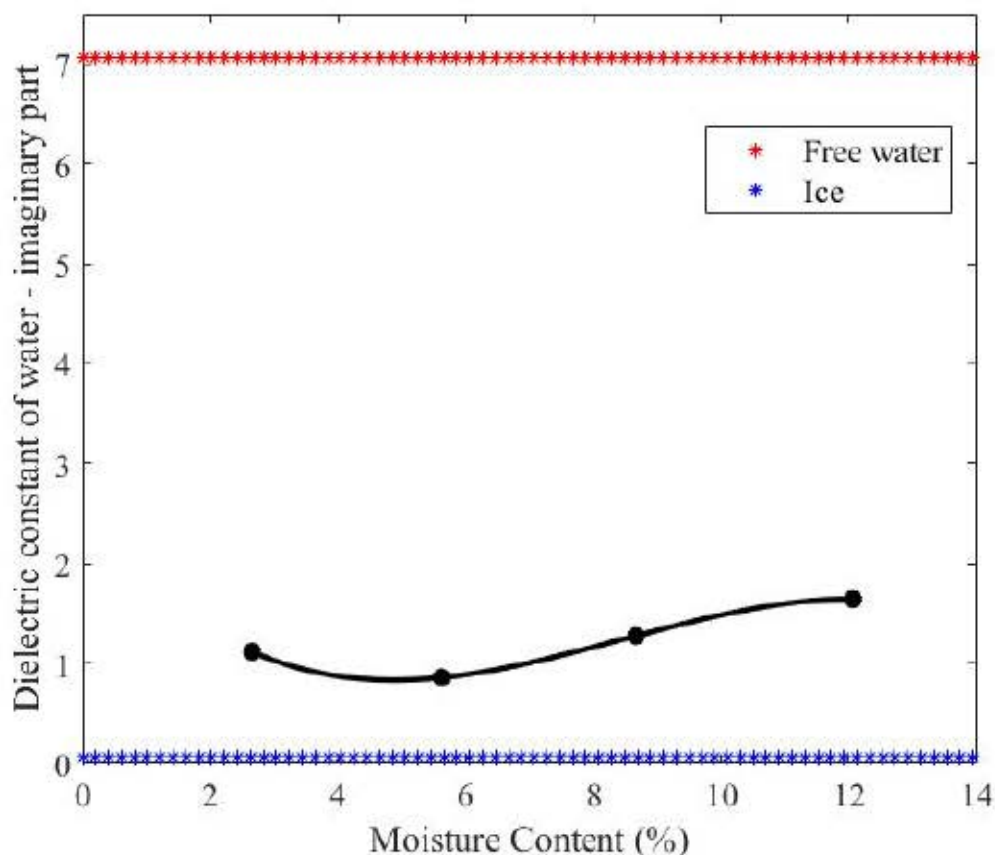


Figure 4.13: Variation of the imaginary part of the dielectric function of water with respect to MC obtained using THz transmission spectroscopy at 0.2 THz.

Chapter 5. The comparison of measurements for the first four MCs are very close to each other (refer to Figure 4.12), with error bars that are relatively large as a result of taking small differences to calculate the dielectric function. According to the data found, the water molecules adsorbed during the initial adsorption process under 12 % behaved almost the same. The transition in the behavior of water molecules was apparent above 12 % as the water molecules started approaching free water like nature. Similarly, a clearer relationship between the imaginary part of the dielectric function can also be made by considering higher MCs in MCC.

The dielectric function also depends on the effective surface area on which the water is adsorbed [19]. It will also be important to see how the dielectric function

of MCC varies with changes in the surface area. To answer this question, one can consider experimenting by taking MCC made from various sources. However, in this thesis, only one type of MCC sample (thus only one source) was used, so the variation of the dielectric constant of MCC with changing the surface area of the sample cannot be predicted. This work could be done in the future, as it is expected that the larger the surface area of the sample, the more capacity the sample has to hold water in the primary sorption sites.

4.5 Summary

In this chapter, we explored the application of THz-TDS to probing water dynamics in the MCC structure. This thesis aimed to address the question of how the transition of the state of water occurs in MCC with a change in MC. It was observed that with an increase in MC, the dielectric function of water is almost constant for low MC and smoothly transitions from irrotational towards free-like behavior with a further increase in MC. The analysis results can be improved with some future work on the study that is defined in Chapter 5 of this thesis.

Chapter 5

Conclusion and Future Directions

In Chapter 4, the real and imaginary parts of the dielectric constant of water at different MCs for the powdered microcrystalline cellulose sample was determined with the help of a simple mixing effective medium model. It was found that both the real and imaginary parts of the dielectric constant of water vary with MC. At low MC, the water molecules were attracted by sorption sites, resulting in very tight hydrogen bonding of the molecules with sites and giving them the characteristics of bound water. As the MC increased, more water molecules were stacked in the secondary layers, which had the characteristics of free and rotational water molecules. Therefore, at low MC, the dielectric constant of water was comparable to the dielectric constant of bound water; at high MC, it started to approach the dielectric constant of water that might be expected for free water. According to our analysis, the transition between the dielectric constants of bound water and free water appeared to begin around 12% MC. For further improvement in the prediction of the dielectric constant of water in MCC, more MCC samples with a higher MC need to be prepared. Preparing more MCs will give us a clear idea about the transition of the water state in MCC from bound to free. As indicated in Figure 4.12, the error bars found in the real part of the dielectric constant of water are

large. Therefore, future work includes improvements to measurement methods to reduce error bars. There are two main ways to reduce those error bars:

- (1) By improving the sample preparation techniques.
- (2) The fundamental precision limit of the THz system used.

In this thesis, the THz sample measurements were taken by rotating Petri dishes four times so that the thickness of the MCC powder in the dish was averaged out. The reason why this was performed is that it was found that the MCC powder was not settled out equally in the Petri dishes. Therefore, to reduce the error due to the change in thickness of the powder in the Petri dish, we took the average of the data collected from the four orientations of the samples. Better methods can be used to settle the powder in the petri dish. As an example, (1) a commercial vibrator or vibrating platform, specifically made to settle the powder, could be used; (2) the time of vibrations could be increased so that it settles the MCC powder evenly in the petri dish. Therefore, to get precise results about the dielectric function of water and reduce its error, the sample preparation methods could be improved.

Also, the precision of our results is fundamentally limited by the precision of the THz system. If we look at the THz time-domain data (in Figure 4.5), the THz time-domain signals are made up of individual data points, and there is coarseness to these data points, which fundamentally limits the precision of our results. Therefore, a THz system with improved temporal sampling can be used to get more precise results.

In this thesis, we were expecting to see the transition of water states in MCC from monomolecular water to polymolecular water to free water. We were able to observe the transition from monomolecular water to polymolecular water molecules (refer to Figures 4.12 and 4.13), but we did not have enough MCs to see the dielectric function of water approaching that of free water. As mentioned in Chapter 4, this could be tested by taking MCs at or above the fiber saturation point.

In this thesis, the MCC powder obtained from a single source was used to study the dielectric constant of water in it. However, this study can be extended to understand the change in the dielectric constant of water in MCC that is obtained from different sources. As the MCC chosen from the different sources will have different effective surface areas, it will be interesting to see how the nature of the dielectric constant of water changes with a change in MC for all the different effective surface areas on which water is adsorbed.

Moreover, in this thesis, the simple effective medium theory model was used. Although the final results of the dielectric constant of water in MCC were not very precise and had large error bars, this model helped us look at the physics behind the interaction of water with cellulose networks. As we need to improve the accuracy of the results in the future anyway, it will make sense to develop a model that correctly identifies the MC-dependent dielectric function in cellulose networks. As described in section 3.4.2 of Chapter 3, there is a large difference in the surface area calculated due to water adsorption as compared to nitrogen adsorption using BET. Therefore, the mechanisms of adsorption of water and nitrogen are quite different from each other. This present study could be expanded to understand the difference between those adsorption processes. Also, the determination of the specific area of water depends on the amount of water adsorbed at the monolayer which again depends on the type of model used. Therefore, with the correct model in the future, we might expect (1) the ability to probe surface area and porosity as an alternative to BET theory and (2) to measure MC more accurately in wood.

Bibliography

- [1] D. Mittleman, *Sensing with terahertz radiation*. Springer, 2013, vol. 85.
- [2] F. Blanchard, G. Sharma, L. Razzari, X. Ropagnol, H.-C. Bandulet, F. Vidal, R. Morandotti, J.-C. Kieffer, T. Ozaki, H. Tiedje, H. Haugen, M. Reid, and F. Hegmann, "Generation of intense terahertz radiation via optical methods," *IEEE Journal of Selected Topics in Quantum Electronics*, vol. 17, no. 1, pp. 5–16, 2011.
- [3] S. Hadjiloucas, L. S. Karatzas, and J. W. Bowen, "Measurements of leaf water content using terahertz radiation," *IEEE Transactions on microwave theory and techniques*, vol. 47, no. 2, pp. 142–149, 1999.
- [4] C. Yu, S. Fan, Y. Sun, and E. Pickwell-MacPherson, "The potential of terahertz imaging for cancer diagnosis: A review of investigations to date," *Quantitative imaging in medicine and surgery*, vol. 2, no. 1, p. 33, 2012.
- [5] L. Wang, "Terahertz imaging for breast cancer detection," *Sensors*, vol. 21, no. 19, p. 6465, 2021.
- [6] D. D. Arnone, C. M. Ciesla, A. Corchia, S. Egusa, M. Pepper, J. M. Chamberlain, C. Bezzant, E. H. Linfield, R. Clothier, and N. Khammo, "Applications of terahertz (thz) technology to medical imaging," in *Terahertz Spectroscopy and Applications II*, vol. 3828. SPIE, 1999, pp. 209–219.
- [7] A. Fitzgerald, E. Berry, N. Zinovev, G. Walker, M. Smith, and J. Chamberlain, "An introduction to medical imaging with coherent terahertz frequency radiation," *Physics in Medicine & Biology*, vol. 47, no. 7, p. R67, 2002.
- [8] S. N. Lowry, B. D. Price, I. D. Hartley, M. R. Shegelski, and M. Reid, "Reflection terahertz time-domain spectroscopy for imaging and identifying concealed interfaces in insulated systems," *Applied Optics*, vol. 60, no. 23, pp. 6818–6828, 2021.
- [9] J. F. Federici, B. Schulkin, F. Huang, D. Gary, R. Barat, F. Oliveira, and D. Zimdars, "Thz imaging and sensing for security applications—explosives, weapons and drugs," *Semiconductor science and technology*, vol. 20, no. 7, p. S266, 2005.

- [10] G. C. Walker, E. Berry, N. N. Zinov'ev, A. J. Fitzgerald, R. E. Miles, J. M. Chamberlain, and M. A. Smith, "Terahertz imaging and international safety guidelines," in *Medical Imaging 2002: Physics of Medical Imaging*, vol. 4682. SPIE, 2002, pp. 683–690.
- [11] M. Reid and R. Fedosejevs, "Terahertz birefringence and attenuation properties of wood and paper," *Applied optics*, vol. 45, no. 12, pp. 2766–2772, 2006.
- [12] T. M. Todoruk, I. D. Hartley, and M. E. Reid, "Origin of birefringence in wood at terahertz frequencies," *IEEE Transactions on Terahertz Science and Technology*, vol. 2, no. 1, pp. 123–130, 2012.
- [13] M. Koch, S. Hunsche, P. Schumacher, M. Nuss, J. Feldmann, and J. Fromm, "Thz-imaging: a new method for density mapping of wood," *Wood Science and Technology*, vol. 32, pp. 421–427, 1998.
- [14] M. Peccianti, R. Fastampa, A. M. Conte, O. Pulci, C. Violante, J. Łojewska, M. Clerici, R. Morandotti, and M. Missori, "Terahertz absorption by cellulose: application to ancient paper artifacts," *Physical Review Applied*, vol. 7, no. 6, p. 064019, 2017.
- [15] D. Fengel and G. Wegener, *Wood: chemistry, ultrastructure, reactions*. Walter de Gruyter, 2011.
- [16] R. Piesiewicz, T. Kleine-Ostmann, N. Krumbholz, D. Mittleman, M. Koch, and T. Kürner, "Terahertz characterisation of building materials," *Electronics Letters*, vol. 41, no. 18, pp. 1002–1004, 2005.
- [17] H. Polge, "Fifteen years of wood radiation densitometry," *Wood Science and Technology*, vol. 12, no. 3, pp. 187–196, 1978.
- [18] B. Goy, P. Martin, and J. Leban, "The measurement of wood density by microwave sensor," *Holz Als Roh-Und Werkstoff*, vol. 50, no. 4, pp. 163–166, 1992.
- [19] B. Ahmed *et al.*, *Determination of density and moisture content of wood using Terahertz time domain spectroscopy*. University of Northern British Columbia, 2015.
- [20] T. Inagaki, B. Ahmed, I. D. Hartley, S. Tsuchikawa, and M. Reid, "Simultaneous prediction of density and moisture content of wood by terahertz time domain spectroscopy," *Journal of Infrared, Millimeter, and Terahertz Waves*, vol. 35, pp. 949–961, 2014.
- [21] D. Saeedkia, *Handbook of terahertz technology for imaging, sensing and communications*. Elsevier, 2013.
- [22] H. Wang, Y. Horikawa, S. Tsuchikawa, and T. Inagaki, "Terahertz time-domain spectroscopy as a novel tool for crystallographic analysis in cellulose," *Cellulose*, vol. 27, pp. 9767–9777, 2020.

- [23] A. Mihranyan, A. P. Llagostera, R. Karmhag, M. Strømme, and R. Ek, "Moisture sorption by cellulose powders of varying crystallinity," *International journal of pharmaceuticals*, vol. 269, no. 2, pp. 433–442, 2004.
- [24] F. S. Vieira and C. Pasquini, "Determination of cellulose crystallinity by terahertz-time domain spectroscopy," *Analytical chemistry*, vol. 86, no. 8, pp. 3780–3786, 2014.
- [25] A. L. Skelbæk-Pedersen, M. Anushek, T. K. Vilhelmsen, J. Rantanen, and J. A. Zeitler, "Non-destructive quantification of fragmentation within tablets after compression from scattering analysis of terahertz transmission measurements," *International Journal of Pharmaceutics*, vol. 588, p. 119769, 2020.
- [26] M. Missori, D. Pawcenis, J. Bagniuk, A. M. Conte, C. Violante, M. S. Maggio, M. Peccianti, O. Pulci, and J. Łojewska, "Quantitative diagnostics of ancient paper using thz time-domain spectroscopy," *Microchemical Journal*, vol. 142, pp. 54–61, 2018.
- [27] T. Hattori, H. Kumon, and H. Tamazumi, "Terahertz spectroscopic characterization of paper," in *35th International Conference on Infrared, Millimeter, and Terahertz Waves*. IEEE, 2010, pp. 1–2.
- [28] B. Carnio, B. Ahvazi, and A. Elezzabi, "Terahertz properties of cellulose nanocrystals and films," *Journal of Infrared, Millimeter, and Terahertz Waves*, vol. 37, pp. 281–288, 2016.
- [29] D. Klemm, B. Heublein, H.-P. Fink, and A. Bohn, "Cellulose: fascinating biopolymer and sustainable raw material," *Angewandte chemie international edition*, vol. 44, no. 22, pp. 3358–3393, 2005.
- [30] V. Kocherbitov, S. Ulvenlund, M. Kober, K. Jarring, and T. Arnebrant, "Hydration of microcrystalline cellulose and milled cellulose studied by sorption calorimetry," *The Journal of Physical Chemistry B*, vol. 112, no. 12, pp. 3728–3734, 2008.
- [31] S. Dumitriu, *Polysaccharides: structural diversity and functional versatility*. CRC press, 2004.
- [32] T. Inagaki, I. D. Hartley, S. Tsuchikawa, and M. Reid, "Prediction of oven-dry density of wood by time-domain terahertz spectroscopy," *Holzforschung*, vol. 68, no. 1, pp. 61–68, 2014.
- [33] D. Grischkowsky, S. Keiding, M. Van Exter, and C. Fattinger, "Far-infrared time-domain spectroscopy with terahertz beams of dielectrics and semiconductors," *JOSA B*, vol. 7, no. 10, pp. 2006–2015, 1990.
- [34] E. Austin, A. Bar-Lev, and J. Everard, "Theoretical study of a double quantum well photoconductive device," *Semiconductor science and technology*, vol. 4, no. 11, p. 931, 1989.

- [35] D. Dragoman and M. Dragoman, "Terahertz fields and applications," *Progress in quantum electronics*, vol. 28, no. 1, pp. 1–66, 2004.
- [36] M. Tani, S. Matsuura, K. Sakai, and S.-i. Nakashima, "Emission characteristics of photoconductive antennas based on low-temperature-grown GaAs and semi-insulating GaAs," *Applied Optics*, vol. 36, no. 30, pp. 7853–7859, 1997.
- [37] Z. Piao, M. Tani, and K. Sakai, "Carrier dynamics and terahertz radiation in photoconductive antennas," *Japanese Journal of Applied Physics*, vol. 39, no. 1R, p. 96, 2000.
- [38] Y.-S. Lee, *Principles of terahertz science and technology*. Springer Science & Business Media, 2009, vol. 170.
- [39] L. Duvillaret, F. Garet, and J.-L. Coutaz, "A reliable method for extraction of material parameters in terahertz time-domain spectroscopy," *IEEE Journal of Selected Topics in Quantum Electronics*, vol. 2, no. 3, pp. 739–746, 1996.
- [40] I. Pupeza, R. Wilk, and M. Koch, "Highly accurate optical material parameter determination with THz time-domain spectroscopy," *Optics Express*, vol. 15, no. 7, pp. 4335–4350, 2007.
- [41] M. Scheller and M. Koch, "Fast and accurate thickness determination of unknown materials using terahertz time domain spectroscopy," *Journal of Infrared, Millimeter, and Terahertz Waves*, vol. 30, pp. 762–769, 2009.
- [42] R. Rowell *et al.*, "The chemistry of solid wood." *The chemistry of solid wood.*, 1984.
- [43] D. Brunick, "Characterization of bimetallic silver-copper nanoinks with hydroxyethyl-cellulose additives," 2022.
- [44] D. Trache, M. H. Hussin, C. T. H. Chuin, S. Sabar, M. N. Fazita, O. F. Taiwo, T. Hassan, and M. M. Haafiz, "Microcrystalline cellulose: Isolation, characterization and bio-composites application—a review," *International Journal of Biological Macromolecules*, vol. 93, pp. 789–804, 2016.
- [45] S. Ardizzone, F. Dioguardi, T. Mussini, P. Mussini, S. Rondinini, B. Vercelli, and A. Vertova, "Microcrystalline cellulose powders: structure, surface features and water sorption capability," *Cellulose*, vol. 6, pp. 57–69, 1999.
- [46] O. Battista and P. Smith, "Microcrystalline cellulose," *Industrial & Engineering Chemistry*, vol. 54, no. 9, pp. 20–29, 1962.
- [47] J. Hogan, P.-I. Shue, F. Podczek, and J. M. Newton, "Investigations into the relationship between drug properties, filling, and the release of drugs from hard gelatin capsules using multivariate statistical analysis," *Pharmaceutical Research*, vol. 13, pp. 944–949, 1996.

- [48] A. Ashori and A. Nourbakhsh, "Performance properties of microcrystalline cellulose as a reinforcing agent in wood plastic composites," *Composites Part B: Engineering*, vol. 41, no. 7, pp. 578–581, 2010.
- [49] W. Bai and K. Li, "Partial replacement of silica with microcrystalline cellulose in rubber composites," *Composites Part A: Applied Science and Manufacturing*, vol. 40, no. 10, pp. 1597–1605, 2009.
- [50] M. H. Schneider, K. I. Brebner, and I. D. Hartley, "Swelling of a cell lumen filled and a cell-wall bulked wood polymer composite in water," *Wood and Fiber Science*, pp. 165–172, 1991.
- [51] I. D. Hartley, "Characterization of water in wood below the fibre saturation point," Ph.D. dissertation, University of British Columbia, 1994.
- [52] G. Zografi and M. J. Kontny, "The interactions of water with cellulose-and starch-derived pharmaceutical excipients," *Pharmaceutical research*, vol. 3, pp. 187–194, 1986.
- [53] I. D. Hartley, F. A. Kamke, and H. Peemoeller, "Cluster theory for water sorption in wood," *Wood Science and Technology*, vol. 26, pp. 83–99, 1992.
- [54] S. Brunauer, P. H. Emmett, and E. Teller, "Adsorption of gases in multimolecular layers," *Journal of the American chemical society*, vol. 60, no. 2, pp. 309–319, 1938.
- [55] L. Stubberud, H. G. Arwidsson, A. Larsson, and C. Graffner, "Water solid interactions ii. effect of moisture sorption and glass transition temperature on compactibility of microcrystalline cellulose alone or in binary mixtures with polyvinyl pyrrolidone," *International journal of pharmaceuticals*, vol. 134, no. 1-2, pp. 79–88, 1996.
- [56] H. Nam-Tran, V. V. Nhuan, M. Buchmann, F. Sabra, P. Ruelle, and U. W. Kesselring, "Adsorption isotherms of water on a set of fractosils and on avicel ph 101r by frontal analysis chromatography," *Drug development and industrial pharmacy*, vol. 19, no. 12, pp. 1413–1445, 1993.
- [57] H. Wang, H. Qian, Y. Gao, and Y. Li, "Classification and physical characteristics of bound water in loess and its main clay minerals," *Engineering Geology*, vol. 265, p. 105394, 2020.
- [58] P. U. Jepsen, U. Møller, and H. Merbold, "Investigation of aqueous alcohol and sugar solutions with reflection terahertz time-domain spectroscopy," *Optics Express*, vol. 15, no. 22, pp. 14717–14737, 2007.
- [59] K. Tielrooij, D. Paparo, L. Piatkowski, H. Bakker, and M. Bonn, "Dielectric relaxation dynamics of water in model membranes probed by terahertz spectroscopy," *Biophysical journal*, vol. 97, no. 9, pp. 2484–2492, 2009.

- [60] I. Grigoriy *et al.*, "Dielectric properties of wood and wood-based materials," 1993.
- [61] J. M. Garnett, "Xii. colours in metal glasses and in metallic films," *Philosophical Transactions of the Royal Society of London. Series A, Containing Papers of a Mathematical or Physical Character*, vol. 203, no. 359-371, pp. 385–420, 1904.
- [62] M. Scheller, S. Wietzke, C. Jansen, and M. Koch, "Modelling heterogeneous dielectric mixtures in the terahertz regime: a quasi-static effective medium theory," *Journal of Physics D: Applied Physics*, vol. 42, no. 6, p. 065415, 2009.
- [63] V. D. Bruggeman, "Berechnung verschiedener physikalischer konstanten von heterogenen substanzen. i. dielektrizitätskonstanten und leitfähigkeiten der mischkörper aus isotropen substanzen," *Annalen der physik*, vol. 416, no. 7, pp. 636–664, 1935.
- [64] D. Aspnes, "Local-field effects and effective-medium theory: a microscopic perspective," *American Journal of Physics*, vol. 50, no. 8, pp. 704–709, 1982.
- [65] M. M. Braun and L. Pilon, "Effective optical properties of non-absorbing nanoporous thin films," *Thin Solid Films*, vol. 496, no. 2, pp. 505–514, 2006.
- [66] G. I. Torgovnikov, *Dielectric properties of wood-based materials*. Springer, 1993.
- [67] D. Aspnes, "Plasmonics and effective-medium theories," *Thin Solid Films*, vol. 519, no. 9, pp. 2571–2574, 2011.
- [68] B. C. Truong, H. D. Tuan, A. J. Fitzgerald, V. P. Wallace, and H. T. Nguyen, "High correlation of double debye model parameters in skin cancer detection," in *2014 36th Annual International Conference of the IEEE Engineering in Medicine and Biology Society*. IEEE, 2014, pp. 718–721.
- [69] D. A. Boyarskii, V. V. Tikhonov, and N. Y. Komarova, "Model of dielectric constant of bound water in soil for applications of microwave remote sensing," *Progress In Electromagnetics Research*, vol. 35, pp. 251–269, 2002.
- [70] E. Pickwell, B. Cole, A. Fitzgerald, V. Wallace, and M. Pepper, "Simulation of terahertz pulse propagation in biological systems," *Applied Physics Letters*, vol. 84, no. 12, pp. 2190–2192, 2004.